International Journal of Greenhouse Gas Control 113 (2022) 103554

Contents lists available at ScienceDirect

International Journal of Greenhouse Gas Control

journal homepage: www.elsevier.com/locate/ijggc

# Direct measurement of $CO_2$ drawdown in mine wastes and rock powders: Implications for enhanced rock weathering

Amanda R. Stubbs [a,*], Carlos Paulo [a], Ian M. Power [a], Baolin Wang [b], Nina Zeyen [b], Sasha Wilson [b]

[a] Trent School of the Environment, Trent University, Peterborough, ON K9L 0G2, Canada
[b] Department of Earth and Atmospheric Sciences, University of Alberta, Edmonton, AB T6G 2E3, Canada

ARTICLE INFO

*Keywords:*
Enhanced rock weathering
Passive carbonation
$CO_2$ fluxes
$CO_2$ sequestration
Kimberlite
Carbon dioxide removal
Negative emission technology

ABSTRACT

Enhanced rock weathering (ERW) sequesters $CO_2$ via solubility and mineral trapping and can be implemented by the mining industry to reduce their net greenhouse gas emissions. Kimberlite residues from Venetia Diamond Mine in South Africa, as well as powdered forsterite, serpentinite, wollastonite skarn, and 10 wt.% brucite mixed with quartz sand, were tested as potential feedstocks for ERW. A $CO_2$ flux system directly measured $CO_2$ removal rates and sensors tracked laboratory conditions and pore water saturation during a series of 2-week experiments. With respect to kimberlites, unweathered residues achieved the greatest drawdown rate of -870 g $CO_2/m^2/yr$ at 48% saturation. In contrast, fine and coarse residues previously exposed to mine process water achieved fluxes of -150 and -160 g $CO_2/m^2/yr$ at 60% saturation. Brucite reached -2940 g $CO_2/m^2/yr$ at 14% saturation compared to forsterite, serpentinite, and wollastonite that achieved fluxes of -500, -260, and -190 g $CO_2/m^2/yr$, respectively, at higher saturations of 53–60%. Mineralogical composition had the greatest effect on $CO_2$ fluxes, followed by water content which drives carbonation reactions and affects permeability. Solid inorganic carbon increased in the brucite, wollastonite, and unweathered kimberlite, indicating that $CO_2$ was stored via mineral trapping as opposed to solubility trapping in the other experiments. Increasing the exposure of unweathered residues, expanding dispersal area, and optimizing water saturation would lead to greater $CO_2$ removal at mine sites.

## 1. Introduction

Atmospheric $CO_2$ has increased from 280 ± 20 ppm in pre-industrial times IPCC, 2007) to 417 ppm in 2020 (NOAA, 2020). In addition to emissions reduction, the United Nations Framework Convention on Climate Change has advised that greenhouse gas (GHG) emissions be stabilized through the use of negative emission technologies (NETs) in an effort to mitigate dangerous interferences to the climate system (EASAC, 2018). Various NETs include afforestation, biochar and soil sequestration, ocean fertilization, bioenergy with carbon capture and storage (BECCS), direct air capture, and most relevant to this study, enhanced rock weathering (ERW; Rosen, 2018). ERW involves spreading of rock powders that contain Ca- and Mg-bearing minerals that react with and sequester $CO_2$. In this process, $CO_2$ from the atmosphere dissolves into pore waters (Eq. 1) and becomes hydrated to form carbonic acid (Eq. 2 and (3), which can be neutralized by reacting with minerals such as forsterite ($Mg_2SiO_4$; Eq. 4).

$$CO_{2(g)} \rightarrow CO_{2(aq)} \quad (1)$$

$$CO_{2(aq)} + H_2O \leftrightarrow H_2CO_{3(aq)} \quad (2)$$

$$H_2CO_{3(aq)} \leftrightarrow HCO_3^- + H^+ \quad (3)$$

$$Mg_2SiO_{4(s)} + 4H^+ \rightarrow 2Mg^{2+} + H_4SiO_4^0 \quad (4)$$

$CO_2$ is trapped as a dissolved phase (e.g., $HCO_3^-$) and later may become mineralized, transitioning to mineral trapping (e.g., $MgCO_3{\cdot}3H_2O$; Eq. 5).

$$Mg^{2+} + CO_3^{2-} + 3H_2O \leftrightarrow MgCO_3{\cdot}3H_2O_{(s)}$$

$$\text{Solubility} \leftrightarrow \text{mineral trapping of } CO_2 \quad (5)$$

ERW can use a variety of minerals and rocks that are applied to natural (e.g., forests) and human-modified environments (e.g., agricultural fields; Beerling et al., 2018; Haque et al., 2019; Schuiling and

* Corresponding author.
*E-mail address:* amandastubbs@trentu.ca (A.R. Stubbs).

https://doi.org/10.1016/j.ijggc.2021.103554
Received 24 May 2021; Received in revised form 3 December 2021; Accepted 7 December 2021
Available online 20 December 2021
1750-5836/© 2021 Elsevier Ltd. All rights reserved.

Krijgsman, 2006; Taylor et al., 2015).

Mafic and ultramafic mine wastes with high surface areas can be used as feedstocks for ERW and $CO_2$ mineralization and have the potential to trap and store substantial amounts of $CO_2$ (Beaudoin et al., 2017; Power et al., 2014; Wilson et al., 2014). Passive carbonation has been documented at chrysotile asbestos (Assima et al., 2012,2014; Beinlich and Austrheim, 2012; Larachi et al., 2010; Levitan et al., 2009; Pronost et al., 2011; Wilson, 2006; Wilson et al., 2009a), nickel (Entezari Zarandi et al., 2017; Wilson et al., 2014), and diamond mines (Mervine et al., 2018; Rollo and Jamieson, 2006; Wilson et al., 2011, 2009b) where weathering of mine waste results in the formation of secondary carbonate minerals, storing $CO_2$ via mineral trapping. Passive carbonation may occur without modification to the mine waste impoundments and can be accelerated by implementing management practices that enhance mineral dissolution and $CO_2$ supply, which are rate-limiting factors in $CO_2$ sequestration (Power et al., 2013). The rate of carbonation in these environments is dependent on four primary factors that include 1) mine waste characteristics (e.g., mineralogy, grain size, and surface area), 2) local climate conditions (e.g., precipitation and temperature), 3) process and pore water chemistry, and 4) the design of storage facilities (Power et al., 2014). Of these four factors, only the storage conditions can be modified to enhance the drawdown of atmospheric $CO_2$ unless considering the use of chemical additives. Therefore, it is essential to understand how modifications to mine waste storage conditions can improve $CO_2$ removal rates to move towards full-scale implementation of ERW.

Assessing and monitoring passive carbonation at mines is challenging as it is time and labor intensive. Detailed surface and depth sampling must be completed on a large number of samples (Wilson et al., 2014). Quantitative mineralogical analyses along with stable and radiogenic carbon isotope data have been used to determine the rate of atmospheric $CO_2$ sequestration and identify carbon sources (Wilson et al., 2011, 2014). However, it can be challenging to differentiate between primary and secondary carbonates at mine sites (Turvey et al., 2018; Wilson et al., 2009a, 2014). Therefore, new methods must be explored. With the ability to measure rates instantaneously, mining companies could routinely monitor and verify $CO_2$ sequestration in their mine waste.

Soil $CO_2$ fluxes have been tracked in various environments, including grasslands, forests, and revegetated mines (Ahirwal et al., 2017; Mukhopadhyay and Maiti, 2014), yet there have been limited studies focusing on measuring $CO_2$ fluxes at mines as a method of quantifying rates of passive carbonation (Lechat et al., 2016; Pronost et al., 2012). In the context of mine waste management, it is important to consider how properties of the feedstock (e.g., mineralogy, particle size, surface area) and those of the porous medium it creates (e.g., water content and permeability) may affect $CO_2$ fluxes.

This study explores the potential for $CO_2$ sequestration via weathering of mine wastes and powdered rocks that are reactive with $CO_2$ and focuses on kimberlite residues from diamond mines. The primary goals of this study are to 1) evaluate various parameters that affect weathering rates (e.g., mineralogy, surface area, particle size, and water content), 2) estimate the rate of $CO_2$ sequestration occurring in wastes from diamond mines under current management practices, and 3) assess how modifications to the management of these wastes could increase $CO_2$ sequestration. To accomplish these goals, laboratory $CO_2$ flux experiments were performed to measure the drawdown of $CO_2$ into different mine wastes and powdered rocks that ranged in reactivity. $CO_2$ fluxes and total inorganic carbon (TIC) may effectively measure $CO_2$ removal rates at mine sites and other ERW applications and aid in understanding how changes in management practices can increase $CO_2$ sequestration.

## 2. Venetia diamond mine description

Kimberlite mine residues from the Venetia Diamond Mine in South Africa have high surface areas due to comminution and an abundance of minerals rich in Ca and Mg, making them desirable for $CO_2$ sequestration (Mervine et al., 2018). At Venetia, the major kimberlite facies mined to date is referred to as massive volcaniclastic kimberlite (MVK). Dark volcaniclastic kimberlite (DVK) is another major facies that is located deeper within the pipes and will be mined more extensively in the future. Kimberlite residues used in this study are from unknown facies unless otherwise stated (e.g., DVK).

There are two fine residue deposits (FRD1 and FRD2), with a total area of approximately 3.5 $km^2$ (Fig. 1); however, only one impoundment is active at any given time. Fine residues (<1 mm) are deposited as a slurry from pipes along the FRD periphery, forming beaches and a pond towards the middle. The deposition points are regularly moved to equally distribute the residues and control the position of the pond. As residues settle, relatively clear water is drained and reused in the processing circuit. Deposition is alternated between the two FRDs to allow for subsidence in the inactive impoundment which gradually dries until no surface water remains.

There is one coarse residues deposit (CRD) which has an area of ~0.5 $km^2$. These residues are 1–8 mm in diameter and are dry-stacked, so there is minimal water in the impoundment. The CRD surface is flat and has sparse grasses and shrubs.

## 3. Methods

### 3.1. Sample acquisition

At Venetia, fieldwork and sampling were conducted in May 2017 and May 2018 on the FRD and CRD impoundments and ore stockpiles (Figs. 1 and 2). The composition of FRD and CRD residues is complicated due to the variety and heterogeneity of the kimberlite pipes, incorporation of country rock during mining, and mixing of kimberlite facies during processing. Kimberlite residues at Venetia are not routinely sampled and analyzed, and therefore, there is little information regarding their composition. A bulk sample (several kilograms) of fine residues was collected as a slurry from one of the outlet pipes at the FRD where some of the fines were lost when excess water was discarded. Bulk samples (several kilograms) of CRD were collected from the deposition point and placed in large plastic bags. Unprocessed DVK rock (several kilograms) was collected from the ore stockpile and further processed in the laboratory. A subset of these samples was characterized and analyzed for their geochemical, mineralogical, and physical properties and used in experiments. Additional samples (9) were collected at surface and depth from FRD1 and FRD2 to understand kimberlite residue heterogeneity and assess whether or not passive carbonation was occurring at Venetia. Detailed field methods are available in the Supplementary Material.

Powdered brucite [$Mg(OH)_2$], quartz ($SiO_2$), forsterite, wollastonite skarn ($CaSiO_3$), and serpentinite [$Mg_3Si_2O_5(OH)_4$] were compared to the more mineralogically complex kimberlite residues. These rock and minerals have been extensively studied as potential feedstocks for $CO_2$ sequestration (Beerling et al., 2018; Harrison et al., 2015; Meysman and Montserrat, 2017; Taylor et al., 2015; Wilson, 2006; Wilson et al., 2010, 2014), with the exception of quartz, which was used as an inert material. Forsterite and quartz sand were purchased from OCL Industrial Materials Ltd and Bell & MacKenzie, Ontario, Canada. Wollastonite skarn samples came from sand-sized soil amendment packages from the Canadian Wollastonite quarry near of Kingston, Ontario, Canada. Brucite ore was sourced from the Brucite Mine, Nevada, United States, and serpentinite was sourced from the Lizard Complex in Cornwall, England, United Kingdom.

### 3.2. Sample characterization

Initial and final TIC (%) were measured for all samples (100 mg) except for CRD due to its heterogeneity using a Model CM5017 Coulometer from UIC Inc. at Trent University. Blanks and calcium carbonate

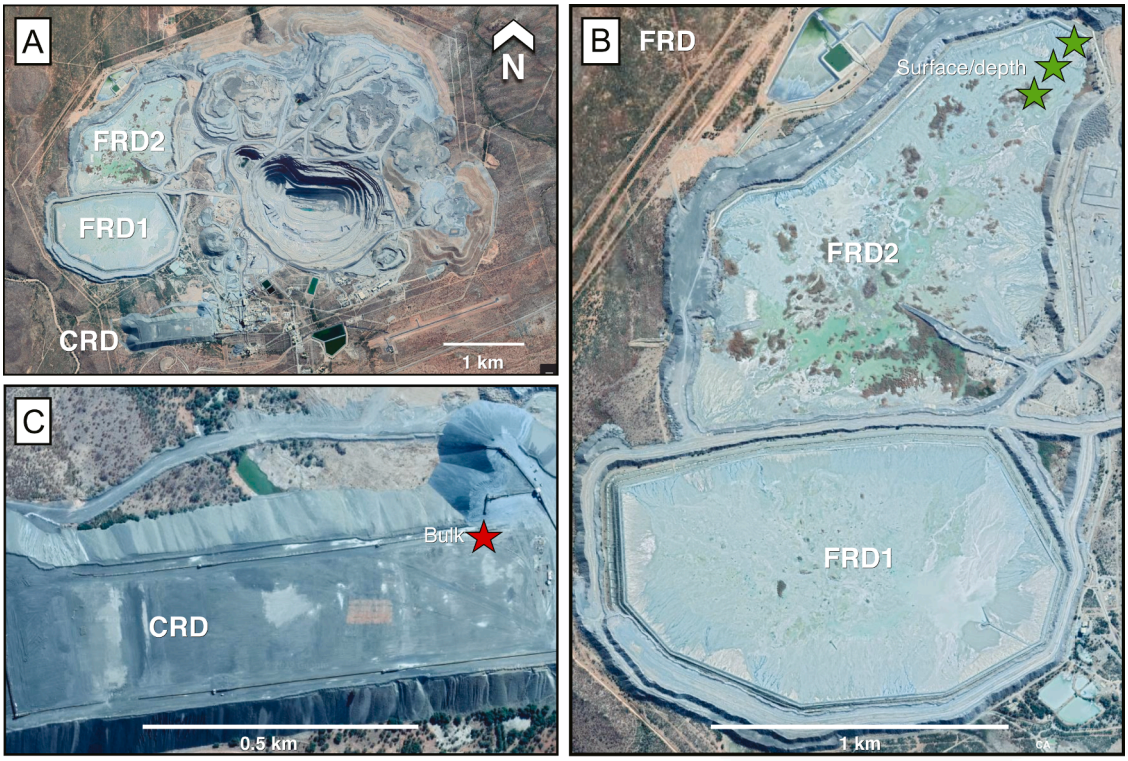


**Fig. 1.** Satellite images of sampling locations from fieldwork conducted in 2017 at the Venetia Diamond Mine, South Africa (**A**). **B:** Sampling locations in FRD1 and FRD2, **C:** Sampling locations of the CRD. Red stars indicate bulk samples, green stars indicate surface and profile samples. (For interpretation of the references to color in this figure legend, the reader is referred to the web version of this article.)

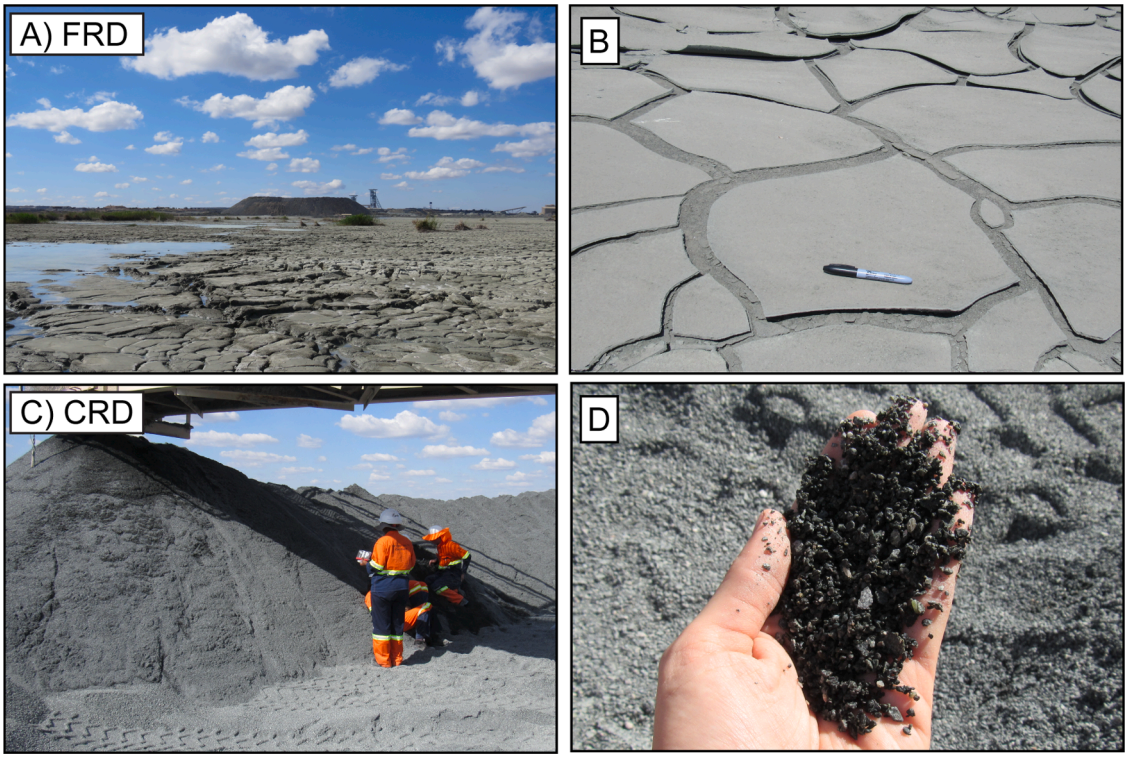


**Fig. 2.** Photographs of sampling locations at Venetia Diamond Mine, South Africa. **A:** FRD ponding to the left and residues drying to the right. **B:** Mud cracks visible on the surface of the FRD (marker for scale). **C:** Location on top of the CRD where sampling of coarse residues (**D**) was conducted.

chelometric standards ($CaCO_3$, Alfa Aesar, 99.95–100.05%) were analyzed before running samples (triplicates) and again every ~15 samples. All samples were micronized for 7 min in anhydrous ethanol using a McCrone Micronizing Mill before analysis to ensure complete reaction of carbonates within the samples. The instrument was set to a temperature of 50 °C and a carrier gas rate of 100 mL/min. Aliquots (10 mL) of 1.0 M $H_2SO_4$ were used to acidify samples for measurements. The pre-scrubber used 15–20 mL of potassium hydroxide (45%) solution to remove any $CO_2$ present in the carrier gas, and the post-scrubber used 10–15 mL of silver nitrate (3%) to remove $H_2S$, $SO_x$, and halogens which can result from the acidification of samples. The cell was filled with a partially aqueous medium containing ethanolamine and a colourimetric indicator. When gas streams enter through this solution, $CO_2$ is quantitatively absorbed and measured. This coulometer is able to measure a TIC range from 0.0001 to 100%. Relative standard deviation was calculated from the analysis of multiple standards and was estimated at 0.53% which validates high analytical precision of the methodology. In addition, samples were analyzed for their bulk geochemical composition using X-ray fluorescence (XRF) spectroscopy by SGS Minerals, Lakefield, Ontario, Canada. Compositions were reported as percent oxides with detection limits ranging from 0.0001–0.01%.

An $N_2$ adsorption method was used to determine Brunauer-Emmett-Teller (BET) specific surface areas at Trent University. Samples were first degassed overnight on a Smart VacPrepTM 067 (Micromeritics, Norcross, GA, USA) that slowly heats to and holds them at 200 °C for 10 h under vacuum. BET analysis was performed at 77 K on the Micromeritics TriStar II Plus adsorption unit (Micromeritics, Norcross, GA, USA) and $N_2$ isotherms were acquired using a $P/P_0$ range of 0.01–0.90. All data processing was done using MicroActive Interactive software (Micromeritics, Norcross, GA, USA). Particle size distributions were obtained using a Horiba LA-950V2 laser-scattering particle size distribution analyzer (Teledyne, USA) and a Vibratory Sieve Shaker AS 200 digit cA (Retsch®).

X-ray diffraction (XRD) patterns were collected under 20–30% relative humidity (RH) using a Bruker D8 Advance θ–θ powder X-ray diffractometer equipped with a LYNXEYE XE-T 1D Position Sensitive Detector in the Environmental Economic Geology Laboratory, University of Alberta, Canada. Mineral phase identification was conducted using the DIFFRAC.EVA XRD phase analysis software (Bruker) with reference to the International Center for Diffraction Data Powder Diffraction File 4+ database (ICDD PDF4+). Rietveld refinements (Bish and Howard, 1988; Hill and Howard, 1987; Rietveld, 1969) with XRD data were used to determine mineral abundances with TOPAS 5 (Bruker). Minerals were categorized as having either a major (10–100 wt.%), minor (1–10 wt.%), or trace (<1 wt.%) abundance. Details for all methods are available in the Supplementary Material.

### 3.3. Experimental methods

#### 3.3.1. Experiment setup

In preparation for $CO_2$ flux experiments, a sample of Venetia DVK ore was crushed (<1.6 cm) and then pulverized (FLSmidth Essa® LM2 Pulverizing Mill) for 5 s to a final particle size similar to that of fine residues (<1 mm; Mervine et al., 2018; Power et al., 2011). Wollastonite skarn, brucite, and serpentinite samples were pulverized for 15, 30, and 40 s, respectively. Different pulverizing times were used to achieve sand-sized particles for wollastonite and serpentinite and fine powder for brucite. The brucite ore (10 wt.%) and quartz sand (90 wt.%) mixture contained 8.28 wt.% brucite as the former was not pure (82.8 wt.%). The CRD from Venetia, as well as quartz and forsterite sand were not modified.

Each experimental setup utilized polyvinyl chloride (PVC) columns (20 cm inner diameter, 10.5 cm height; Fig. 3) inserted into a PVC base to ensure no air escaped at the base of the column during measurements. Residues and powdered rocks were thoroughly homogenized and then added into a column as ~2 cm layers with water to a thickness of 8.5 cm. This helped achieve 60% saturation throughout the column. The mass required depended on the sample density ($\rho_{sample}$) and grain size; however, every experiment had a thickness of 8.5 cm and an exposed sample area of 320 $cm^2$. All experimental columns had 2700 $cm^3$ of occupied material and a 2 cm offset as recommended by LI-COR Biosciences, which is used to determine the total volume of air inside the column.

The bulk volume ($V_{bulk}$; Eq. 6) and density ($\rho_{bulk}$; Eq. 7) that includes voids were calculated to determine the porosity (Φ; Eq. 8) of the residues

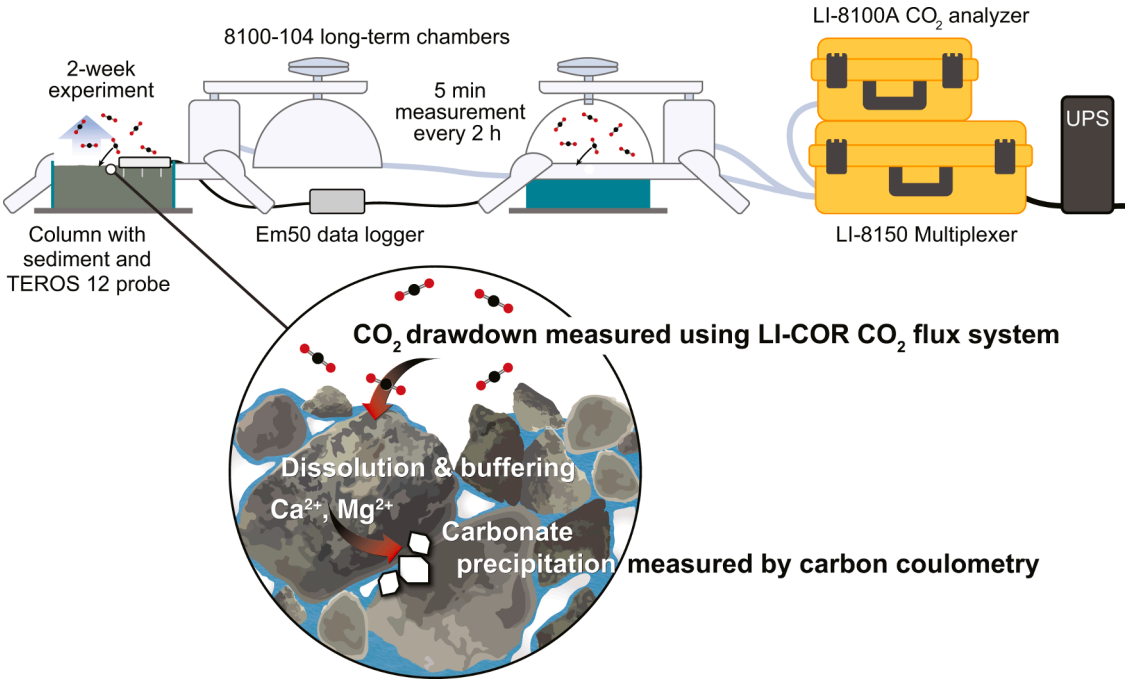


**Fig. 3.** Experimental setup for $CO_2$ flux measurements using an LI-8100A automated soil $CO_2$ flux system coupled with an LI-8150 multiplexer and two 8100–104 long-term chambers (Modified from LI-COR). Sample temperature, electrical conductivity, and volumetric water content were measured using TEROS 12 soil probes and an Em50 Data Logger that recorded values every 15 min. Total inorganic carbon was measured by coulometry.

and powdered rocks:

$$V_{bulk} = \pi r^2 \times h \tag{6}$$

$$\rho_{bulk} = \frac{m_{sample}}{V_{bulk}} \tag{7}$$

$$\Phi = 1 - \frac{\rho_{bulk}}{\rho_{sample}} \tag{8}$$

where $r$ is the column radius (cm), $h$ is the sediment thickness (cm), $m_{sample}$ is the sample mass (g), and $\rho_{sample}$ is the density (g/cm$^3$) of the residues and powdered rocks. For powdered rocks, $\rho_{sample}$ is the density of the dominant mineral and for Venetia residues, $\rho_{sample}$ was calculated based on mass and volume measurements. The volume of solids (Eq. 9) and voids (Eq. 10) were calculated to determine the volume of water needed to achieve a saturation of 60% (Eq. 11) and corresponding volumetric water content (Eq. 12; Table 1):

$$V_{solids} = \frac{m_{sample}}{\rho_{sample}} \tag{9}$$

$$V_{voids} \quad V_{bulk} \quad V_{solids} \tag{10}$$

$$V_{H_2O} = V_{voids} \times \ 0.60 \tag{11}$$

$$VWC\ (\%) = \frac{V_{H_2O}}{V_{bulk}} \times 100\% \tag{12}$$

where $V_{solids}$ is the volume (cm$^3$) of the solid residues and powdered rocks (excludes voids), $V_{voids}$ is the volume (cm$^3$) of voids in the sediment, $V_{H_2O}$ is the volume (cm$^3$) of water added to achieve 60% saturation, and $VWC$ is the volumetric water content (%). An initial water saturation of 60% was selected as the high-end of the optimal range (30–60%) for carbonation (Assima et al., 2013; Harrison et al., 2015). Sediments were allowed to dry during the experiment, thereby passing through the optimal water saturation. Deposited experiments refer to material that was flat, similar to what was observed at Venetia, whereas tilled experiments refer to material that was overturned using a spatula to increase the exposure of sediments to air. In the tilled experiments, sediments were overturned once after the addition of water for the first time, with the exception of forsterite, which was never tilled. In the Venetia FRD experiment the residues were overturned after 28 days (two wetting and drying cycles) and in the DVK experiment, after 14 days.

### 3.3.2. $CO_2$ flux measurements

$CO_2$ flux measurements were carried out under laboratory conditions with an LI-8100 automated soil $CO_2$ flux system coupled with an LI-8150 multiplexer and two 8100–104 long-term chambers (Fig. 3; LI-COR, Lincoln, Nebraska, USA). This equipment allowed for automated consecutive flux measurements of the powdered rocks and kimberlite residues over time. The rate of change in $CO_2$ concentration inside the long-term chamber determines the $CO_2$ diffusion rate (μmol/m$^2$/s). In this study, negative fluxes indicate uptake of $CO_2$ (ingress), whereas positive fluxes indicate the release of $CO_2$ (efflux) from samples. Sample temperature ( °C), electrical conductivity (mS/cm) and volumetric water content (%VWC) were measured using TEROS 12 soil moisture probes that recorded values every 15 min. In addition, a YesAir air quality monitor from Critical Environment Technologies™ was used to track room temperature and relative humidity (RH). A computer and the $CO_2$ flux system were plugged into an uninterrupted power supply (900 W capacity) connected to backup power.

The instrument was programmed to measure fluxes every 2 h for 5 min (300 s) with a 5-min post purge. Dry fluxes were measured for 2 days prior to the addition of water. Afterwards, each experiment ran for 14 days before tilling or additional wettings (Table 1). Deionized water (pH = 5.6) used in experiments was at equilibrium with atmospheric $CO_2$. All experiments, except for forsterite, were wetted only once at the beginning to determine the ideal water content for $CO_2$ drawdown. Water was added to the forsterite experiments once per day for 7 days to determine if reactivity was maintained during repeated wettings. The sediments were then allowed to dry for one week. Duplicates were run for all experiments with the exception of DVK and serpentinite due to limited sample mass.

For the first runs of the brucite-quartz mixture and the forsterite experiments, the 8100–104 long-term chamber was connected directly to the LI-8100 $CO_2$ gas analyzer, while the second run was connected to the LI-8150 multiplexer. Slightly more negative fluxes were recorded when the long-term chamber was connected directly to the gas analyzer due to different relative humidity in the laboratory.

### 3.3.3. Data processing

$CO_2$ flux data were processed using SoilFluxPro 4.0.1, an application for viewing and processing data from the LI-8100 system. $CO_2$ flux results from all experiments were fitted to an exponential curve except for the brucite-quartz experiment, which was fitted to a linear trend. Each flux was calculated based on the change in $CO_2$ concentration from 50–250 s of the 300 s measurement. Flux measurements that yielded empirical fits with an $R^2$ value <0.5 were removed. Outliers were determined by calculating the 1st and 3rd quartile, interquartile ranges, lower and upper bound of data, and selecting any data points that fit in this range.

### 3.3.4. Sampling and characterization

After each experiment, the residues and powdered rocks were cored ($n = 3$) with samples taken at the top 0.5 cm, middle 3–4 cm, and bottom 8 cm. All samples were then analyzed for TIC using the previously described methods. Powdered rocks and minerals that increased in TIC were analyzed by XRD using a Bruker D2 Phaser X-ray diffractometer, and secondary carbonates were identified using DIFFRAC.EVA. Secondary precipitates that formed on the FRD and CRD surfaces were

**Table 1**
Physical properties for each experiment. Duplicate runs were completed for each experiment except for quartz, serpentinite, and DVK due to limited mass.

| Sample | Mass (g) | Number of wettings | Sediment thickness (cm) | Bulk density (g/cm$^3$) | Sample density (g/cm$^3$) | Porosity (%) | Solids volume (cm$^3$) | Void volume (cm$^3$) | $H_2O$ (mL) | VWC (%) | Initial saturation (%) | Initial TIC(%) | Final TIC (%) |
|---|---|---|---|---|---|---|---|---|---|---|---|---|---|
| Quartz | 4522 | 2 | 8.5 | 1.69 | 2.65 | 36 | 1707 | 963 | 578 | 21.6 | 60 | 0.00 | 0.00 |
| 10 wt.% brucite + 90 wt.% quartz | 4525 | 1 | 8.5 | 1.69 | 2.65 | 36 | 1708 | 961 | 577 | 21.6 | 60 | 0.12 | 0.14 |
| Forsterite | 5920 | 7 | 8.5 | 2.22 | 3.32 | 33 | 1783 | 886 | 531 | 19.9 | 60 | 0.02 | 0.02 |
| Serpentinite | 4213 | 1 | 8.5 | 1.58 | 2.57 | 39 | 1639 | 1030 | 618 | 23.2 | 60 | 0.01 | 0.01 |
| Wollastonite skarn | 4810 | 1 | 8.5 | 1.8 | 2.98 | 40 | 1614 | 1055 | 633 | 23.7 | 60 | 0.24 | 0.28 |
| CRD | 4570 | 3 | 8.5 | 1.71 | 2.86 | 40 | 1598 | 1071 | 643 | 24 | 60 | N/A | N/A |
| FRD | 4258 | 3 | 8.5 | 1.6 | 2.58 | 38 | 1650 | 1019 | 611 | 22.9 | 60 | 0.46 | 0.46 |
| DVK | 4522 | 2 | 8.5 | 1.69 | 2.62 | 35 | 1726 | 943 | 566 | 21.2 | 60 | 0.43 | 0.64 |

sampled using tweezers and examined using scanning electron microscopy (SEM) at The University of Western Ontario in the Nanofabrication Facility in London, Ontario, Canada. Samples were mounted onto aluminum stubs using 12 mm carbon adhesive tabs and coated using a Filgen osmium plasma coater (OPC 80T) that applied 10 nm of osmium metal. A LEO (Zeiss) 1540 XB field emission SEM with a secondary electron detector was used to produce high-resolution images at an operating voltage of 1.0 kV, and an Oxford Instruments X-max 50 energy dispersive spectrometer (EDS) was utilized for elemental analysis at an operating voltage of 10.0 kV and a working distance of 4 mm.

#### 3.3.5. Slurry pH measurements

The pH of slurries made from residues and powdered rocks was measured to approximate the pH of the pore waters in the experiments. Aliquots (25 g) of each sample were thoroughly mixed with 10 mL of deionized water (pH = 5.6) in 50 mL plastic centrifuge tubes. Solution pH was measured 1 h after mixing and again after 5 days using an Orion Star A321 pH meter.

## 4. Results

### 4.1. Quartz

Quartz sand (100 wt.% quartz; Table 2) was tested to show the variability of $CO_2$ flux measurements for an unreactive material. The sand had a low surface area (0.09 $m^2/g$) as it was dominated by sand-sized particles (Table 3). During the dry run, the temperature ranged from 21 to 31 °C and the RH ranged from 40 to 65%. Dry quartz sand exhibited an average flux of 10 ± 117 g $CO_2/m^2/yr$ (Fig. 4A). After water addition, there was little change in the $CO_2$ fluxes, which were between -66 to 210 g $CO_2/m^2/yr$ with an average of 80 g $CO_2/m^2/yr$ (Fig. 4A). During this time, the temperature ranged from 21–32 °C and RH ranged from 28 to 85%. No TIC was detected in the quartz sand ($n$ = 3) upon completion of experiments, with values remaining at 0%.

**Table 2**
Quantitative mineralogy for powdered rocks as determined by Rietveld refinement of XRD data.

| Sample | Powdered rocks |
|---|---|
| Quartz | 100.0 wt.% quartz |
| Brucite | 82.8 wt.% brucite; 6.0 wt.% hydromagnesite; 5.1 wt.% dolomite; 2.5 wt.% forsterite; 2.0 wt.% magnetite; 0.6 wt.% pyroaurite; 0.5 wt.% clinochlore; 0.4 wt.% lizardite; 0.2 wt.% quartz |
| Forsterite | 74.1 wt.% forsterite; 19.6 wt.% lizardite; 3.9 wt.% enstatite; 1.4 wt.% magnetite; 1.1 wt.% quartz |
| Serpentinite | 93.2 wt.% lizardite; 2.4 wt.% forsterite; 2.4 wt.% hematite; 1.1 wt.% brucite; 0.9 wt.% clinochlore |
| Wollastonite skarn | 41.0 wt.% diopside; 21.6 wt.% wollastonite; 12.1 wt.% orthoclase; 11.3 wt.% albite; 10.7 wt.% quartz; 2.8 wt.% calcite; 0.6 wt.% muscovite |

### 4.2. Brucite and quartz

The mixture of 10 wt.% brucite + 90 wt.% quartz (Fig. 5A) exhibited the most negative $CO_2$ flux from all experiments. The brucite (82.8 wt.%) sample contained minor abundances of hydromagnesite, dolomite, forsterite, and magnetite (Table 2). The median grain size for the pulverized brucite was 8 μm, and it had a specific surface area of 5.29 $m^2/g$ (Table 3). The pulverized brucite was mixed with quartz sand (90 wt.%) that was used in the quartz experiments. Over 2 days of dry measurements, the temperature ranged from 22 to 24 °C, RH ranged from 16 to 25%, and the $CO_2$ fluxes averaged 20 ± 140 g $CO_2/m^2/yr$. Both experimental runs started at 60% saturation after water addition and decreased to 10% after 14 days. The laboratory conditions during runs 1 and 2 were fairly consistent, with temperature ranging between 20 and 24 °C and RH ranging from 8–40%. The average $CO_2$ flux was -550 g $CO_2/m^2/yr$ during the first day, becoming more negative, reaching -900 g $CO_2/m^2/yr$ over the following 3 days. From day 4 to 7, $CO_2$ fluxes became more negative, decreasing from -940 to -2940 g $CO_2/m^2/yr$. Run 2 showed a similar trend to the first experiment (Fig. 5B); however, it exhibited slightly less negative fluxes. After 14 days, the average TIC increased from 0.12% (±SD 0.01%) to 0.14% (±SD 0.01%; $n$ = 24)

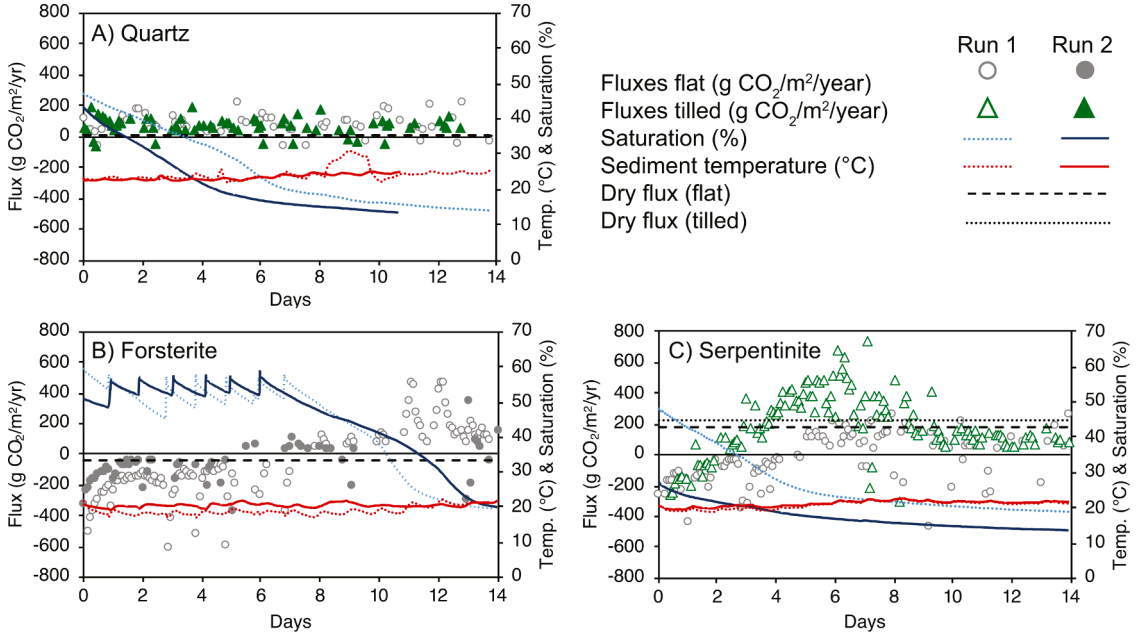


**Fig. 4.** $CO_2$ fluxes (g $CO_2/m^2/yr$) for quartz (**A**), forsterite (**B**), and serpentinite (**C**). Open and solid gray circles represent runs 1 and 2 of the deposited (flat surface) experiments, respectively. Open and solid green triangles represent runs 1 and 2 of the tilled experiments, respectively. Positive values indicate efflux of $CO_2$, while negative values show ingress of $CO_2$. The forsterite experiment included seven wetting and drying cycles to examine changes in reactivity. (For interpretation of the references to color in this figure legend, the reader is referred to the web version of this article.)

**Table 3**
Particle sizes of powdered rocks and Venetia residues separated by clay, silt, sand, and pebbles as well as BET surface area.

| Sample | Clay (%) <0.002 mm | Silt (%) 0.002–0.05 mm | Sand (%) 0.05–2.0 mm | Pebbles (%) >2.0 mm | D50 (μm) | BET ($m^2$/g) |
|---|---|---|---|---|---|---|
| Quartz | 2.0 | 32.4 | 65.6 | 0.0 | 329 | 0.09 |
| Brucite | 21.0 | 57.9 | 21.1 | 0.0 | 8 | 5.29 |
| Forsterite | 4.3 | 25.7 | 69.9 | 0.0 | 264 | 1.14 |
| Serpentinite | 9.4 | 42.8 | 47.9 | 0.0 | 41 | 25.30 |
| Wollastonite skarn | 3.4 | 43.6 | 53 | 0.0 | 52 | 0.87 |
| CRD | 0.0 | 0.0 | 30.9 | 69.1 | 3000 | 5.80 |
| FRD | 0.8 | 9.0 | 89.7 | 0.5 | 550 | 7.70 |
| DVK | 6.4 | 33.6 | 60.0 | 0.1 | 140 | 18.30 |

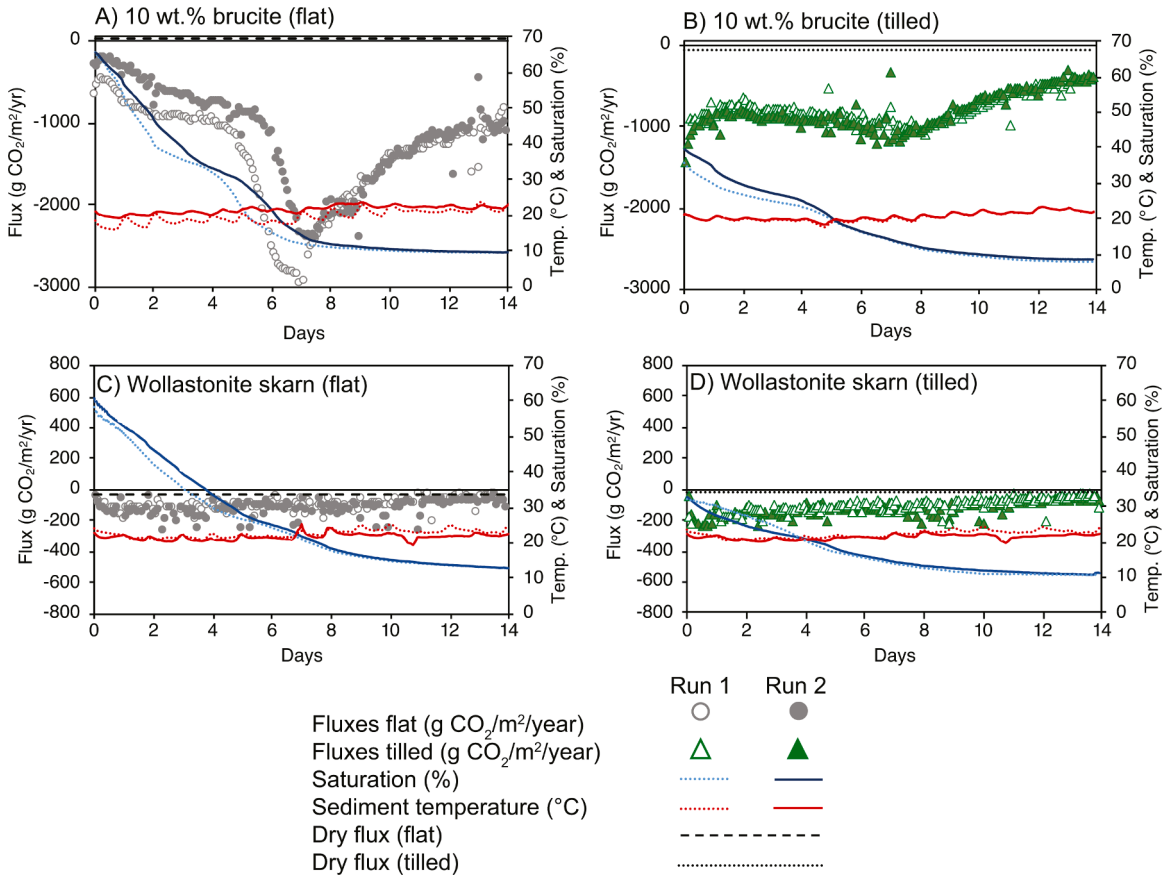


**Fig. 5.** $CO_2$ fluxes (g $CO_2$/$m^2$/yr) for reactive powdered rocks: flat (**A**) and tilled (**B**) brucite-quartz mixtures, and flat (**C**) and tilled (**D**) wollastonite. Open and solid gray circles represent runs 1 and 2 of deposited (flat surface) experiments, respectively. Open and solid green triangles represent runs 1 and 2 of the tilled experiments, respectively. (For interpretation of the references to color in this figure legend, the reader is referred to the web version of this article.)

while surface (0–1 cm) samples generally showed the greatest change, up to a maximum of +0.07%. The most prominent X-ray diffraction peaks for hydromagnesite [$Mg_5(CO_3)_4(OH)_2{\cdot}4H_2O$] were more intense after 14 days indicating the formation of secondary hydromagnesite.

Initial fluxes for the tilled brucite experiment were approximately twice that of the flat experiments, reaching rates of -1220 and -1460 g $CO_2$/$m^2$/yr for runs 1 and 2, respectively (Fig. 5B). Although the same amount of water was added to experiment types to achieve 60% saturation, the readings were underestimated in the tilled experiments due to poor contact between the sediment and moisture probes. The initial saturation reading was 38%, decreasing to 9% after 14 days. Fluxes increased logarithmically after a day and a half, reaching -800 g $CO_2$/$m^2$/yr at ~30% saturation. During day 2, fluxes slowly became more negative, reaching -1200 g $CO_2$/$m^2$/yr at 14% saturation by the end of day 7. As evaporation progressed, fluxes became less negative, reaching -390 g $CO_2$/$m^2$/yr by day 14 (Fig. 5B).

### 4.3. Forsterite

Forsterite (74.1 wt.%) sand contained a major abundance of lizardite (19.6 wt.%) with minor enstatite, magnetite, and quartz (Table 2). This material had a median grain size of 264 μm and a specific surface area of 1.14 $m^2$/g (Table 3). During the initial dry period, the average flux was -40 ± 11 g $CO_2$/$m^2$/yr, and laboratory temperature and RH ranged from 22 to 24 °C and 16–25%, respectively. The two forsterite runs showed similar trends (Fig. 4B), yet $CO_2$ fluxes were slightly shifted due to differences in RH, as was observed in the brucite experiments. Laboratory temperature ranged from 20 to 24 °C, and RH from 8 to 40%. Fluxes were most negative after the first water addition, reaching -500 and -330 g $CO_2$/$m^2$/yr for runs 1 and 2, respectively, and then shifted to near-zero values after 1 day of drying. Additional wettings drove $CO_2$ removal; however, fluxes were less negative with each subsequent water addition. For example, in run 1, the flux was -270 g $CO_2$/$m^2$/yr after 3rd water addition compared to -120 g $CO_2$/$m^2$/yr after the last water

addition. After seven wetting and drying cycles, the forsterite sediments were allowed to dry to 20% saturation (Fig. 4B). During this drying period, $CO_2$ fluxes became increasingly positive, reaching positive fluxes of 470 g $CO_2/m^2/yr$. Diurnal fluctuations in temperature ranged from 17 to 23 °C, with the warmest time of day resulting in more positive fluxes than cooler periods. No differences in TIC ($n = 24$) were measured for forsterite samples.

### 4.4. Serpentinite

Serpentinite was mainly comprised of lizardite (93.2 wt.%) with minor amounts of hematite, forsterite, and brucite (Table 2). This pulverized material had a median grain size of 41 μm and a specific surface area of 25.30 $m^2/g$ (Table 3). Dry fluxes averaged 180 ± 170 and 220 ± 160 g $CO_2/m^2/yr$ for the flat and tilled experiments, respectively. During this dry period, the lab temperature stayed at 22 °C and RH ranged from 15 to 26%. The most negative fluxes were recorded immediately after water addition, reaching -260 and -270 g $CO_2/m^2/yr$ for the flat and tilled experiments, respectively (Fig. 4C). Flat sediments exhibited a more extended period with negative $CO_2$ fluxes from 0 to 5 days, corresponding to a decline in water saturation from 48% to 25%. In the tilled experiment, negative fluxes were only observed from 0 to 2 days at 22–27% water saturation. Fluxes became increasingly positive after days 2 and 4 for the tilled and flat experiments, respectively. During these runs, the temperature ranged from 22 to 23 °C and RH ranged from 12 to 36%. No changes in inorganic carbon were detected for the serpentinite flat ($n = 9$) and tilled ($n = 9$) experiments with TIC remaining at 0.01%.

### 4.5. Wollastonite skarn

The wollastonite skarn contained major abundances of wollastonite (21.6 wt.%), diopside ($CaMgSi_2O_6$; 41.0 wt.%), orthoclase, albite, and quartz and minor amounts of calcite (Table 2). This material had a median grain size of 52 μm and a specific surface area of 0.87 $m^2/g$ (Table 3). The initial dry periods for the flat and tilled experiments had average fluxes of -30 ± 50 and 20 ± 70 g $CO_2/m^2/yr$, respectively. Flat experiments exhibited a negative flux of -50 g $CO_2/m^2/yr$ after water addition and reached the most negative flux of -190 g $CO_2/m^2/yr$ after a day of drying (53% saturation). During the following 13 days, fluxes slowly became less negative (Fig. 5C). Tilled experiments exhibited the most negative flux during the first day immediately after the addition of water, reaching -200 g $CO_2/m^2/yr$ at approximately 33% saturation (Fig. 5D). As sediments dried, fluxes became less negative, reaching values of -40 and -50 g $CO_2/m^2/yr$ for runs 1 and 2, respectively. TIC increased from 0.24% (±SD 0.04%) to 0.28% for flat ($n = 16$) and tilled wollastonite ($n = 18$), respectively. X-ray diffraction peaks for calcite ($CaCO_3$) in the final solids were more intense, indicating secondary calcite formation.

### 4.6. Venetia residues

The Venetia kimberlite residues contained 47% $SiO_2$, 17% MgO, and 7% CaO, falling within the ranges of all Venetia samples analyzed in this study ($SiO_2 = 40.3–48.7\%$; $MgO = 14.0–25.2\%$; $CaO = 5.7–8.1\%$; Table S1). The CRD and FRD residues were comprised of minerals (Table 4) that are desirable for $CO_2$ sequestration including lizardite (23.1 and 19.3 wt.%), diopside (13.2 and 9.8 wt.%), and clinochlore (6.8 and 4.7 wt.%). Initial TIC of the CRD and FRD residues was 0.53% and 0.46%, equivalent to 4.4 wt.% and 3.8 wt.% calcite, respectively, which is similar to the abundances of calcite quantified using XRD data (3.8–7.0 wt.%; Table S2). The bulk CRD and FRD samples had median grain sizes of 3 mm and 550 μm with surface areas of 5.8 and 7.7 $m^2/g$, respectively (Table 3). Surface and depth samples had broader abundances of minerals of interest: 12.0–33.1 wt.% lizardite, 7.2–19.3 wt.% diopside, and 4.7–8.8 wt.% clinochlore (Table S2).

Dry $CO_2$ fluxes of the CRD and FRD both averaged -80 g $CO_2/m^2/yr$ (Fig. 6). More negative fluxes were recorded after water addition; however, fluxes became much less negative within the first day. Initial wet fluxes for both CRD runs were -140 g $CO_2/m^2/yr$ (Fig. 6A) and were -90 and -180 g $CO_2/m^2/yr$ for FRD runs 1 and 2 (Fig. 6B). As evaporation continued, diurnal temperature fluctuations caused $CO_2$ fluxes to increase and decrease with cooler and warmer temperatures, respectively. The CRD experiment had an immediate drawdown after adding water in the second wetting period, reaching -130 g $CO_2/m^2/yr$ in run 1, similar to the first wetting period (Fig. 6C). Measurements were overestimated in the CRD despite adding the same volume of water as the FRD however, pore water saturation data using coarse material may not be reliable due to poor contact between the sediment and sensor. During the second wetting period of the FRD experiment, there were minimal changes in $CO_2$ fluxes (Fig. 6D). The CRD was wetted for a third time causing the flux to reach values of -200 and -180 g $CO_2/m^2/yr$ in runs 1 and 2 immediately after water addition (Fig. 6E). The most negative $CO_2$ fluxes of the FRD and CRD experiments were recorded in the FRD tilled experiment (final wetting period) with values of -280 g $CO_2/m^2/yr$ ($n = 2$; Fig. 6F). Diurnal temperature fluctuations caused $CO_2$ fluxes to vary with some becoming substantially more negative for short periods of time. Due to the coarse grain size of CRD, representative samples for TIC were not obtainable. No changes were detected in TIC for FRD experiments ($n = 5$).

Mud cracks developed in the fine residues as they dried, and sparse white efflorescent crusts (<1 mm) formed on the surface (Fig. 7A). These precipitates appeared as slender, prismatic crystals under SEM (~3 × 1 μm; Fig. 7B). Some precipitates were also observed within the top ~1 cm of CRD residues (Fig. 7C) and appeared as nodules with some elongated crystals (~2 × 1 μm; Fig. 7D) when viewed using SEM. These white efflorescence crusts are similar to those observed at Venetia on the surfaces of exposed fine residues (Fig. 7E). EDS analyses of these precipitates showed they contained high but variable abundances of Na, Ca, S, O, and C, suggesting these may be mixtures of sulfate and carbonate minerals.

DVK contained 40% $SiO_2$, 25% MgO, and 6% CaO and its mineralogical composition differed from the MVK-dominated CRD and FRD with only lizardite (33.1 wt.%) and diopside (15.6 wt.%) being present as minerals of interest for $CO_2$ sequestration (Table 4). After being pulverized to match the distribution of the FRD, DVK had a median grain size of 140 μm and a specific surface area of 18.3 $m^2/g$ (Table 3), greater than that of FRD (7.7 $m^2/g$).

During the first day of dry measurements, the average flux was -1320 g $CO_2/m^2/yr$ and became less negative during the second day averaging -790 g $CO_2/m^2/yr$ (Fig. 6G). Upon water addition, fluxes were less negative at -630 g $CO_2/m^2/yr$ and became less negative by the start of day 2. A parabolic trend was observed in the $CO_2$ fluxes for the remainder of the experiment. As the residues dried from 54% to 41%

**Table 4**
Quantitative mineralogy (wt.%) of Venetia residues. Minerals identified included Cal – calcite, Di – diopside, Or – orthoclase, Phl – phlogopite, Clc – clinochlore, talc, Qtz – quartz, Tr- tremolite, Ab – albite, Lz – lizardite, and Sme – smectite. Rwp represents the weighted profile residual, a function of the least squares residual (%).

| Sample | Cal | Di | Or | Phl | Clc | Talc | Qtz | Tr | Ab | Lz | Sme | Total | Rwp (%) |
|---|---|---|---|---|---|---|---|---|---|---|---|---|---|
| CRD | 5.2 | 13.2 | 4.4 | 7.0 | 6.8 | 2.5 | 5.5 | 9.0 | 11.0 | 23.1 | 12.3 | 100 | 7.9 |
| FRD | 4.9 | 9.8 | 4.2 | 17.8 | 4.7 | 4.6 | 4.0 | 5.1 | 7.2 | 19.0 | 18.8 | 100 | 12.4 |
| DVK | 4.4 | 15.6 | 0.0 | 16.6 | 0.0 | 0.0 | 0.0 | 2.3 | 0.0 | 33.1 | 28.1 | 100 | 10.4 |

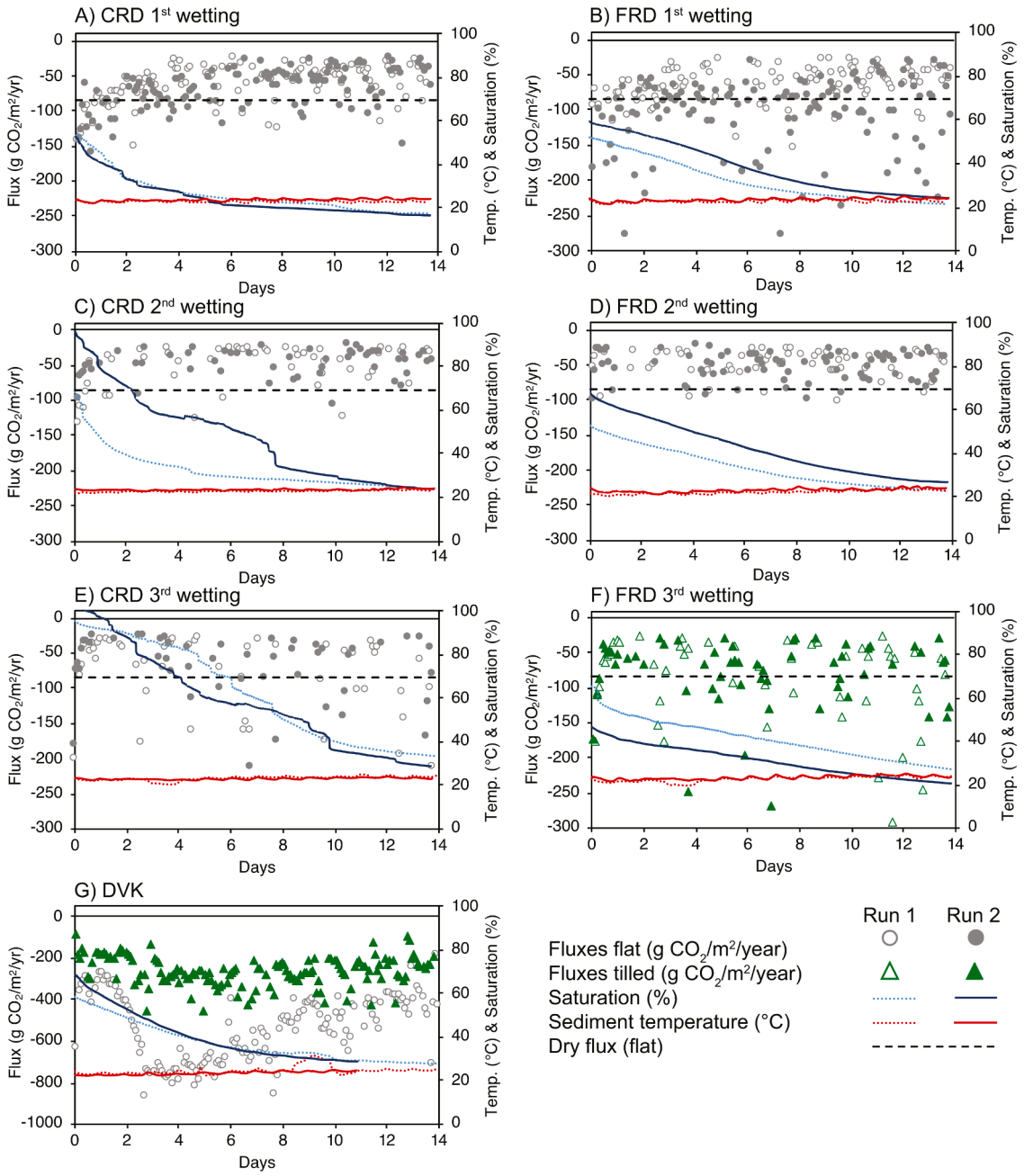


**Fig. 6.** $CO_2$ fluxes (g $CO_2/m^2/yr$) for Venetia residues. **A:** CRD 1st wetting, **B:** FRD 1st wetting, **C:** CRD 2nd wetting, **D:** FRD 2nd wetting, **E:** CRD 3rd wetting **F:** FRD 3rd wetting (tilled), **G:** DVK. Open and solid gray circles represent runs 1 and 2 of the deposited (flat surface) experiments. Open and solid green triangles represent runs 1 and 2 of the tilled experiment.

saturation during days 1 to 4, fluxes became more negative to -870 g $CO_2/m^2/yr$ between days 2 and 3 (Fig. 6G). Further drying caused fluxes to become less negative, returning to values observed during day 1. After 14 days, the DVK was wetted for a second time and then tilled; however, only minor differences in fluxes were observed at different water contents. Fluxes recorded during the first two days averaged -190 g $CO_2/m^2/yr$, becoming more negative as the sample continued to dry, when the most negative flux was -450 g $CO_2/m^2/yr$ (Fig. 6G). TIC ($n = 6$) increased by 0.21% from 0.43% (±SD 0.004%) to 0.64% (±SD 0.001%).

## 5. Discussion

### 5.1. Effect of mineral dissolution rates on $CO_2$ fluxes

Mineralogical composition is a crucial property that often determines the suitability of a prospective feedstock for enhanced weathering and $CO_2$ mineralization (Power et al., 2013). Specifically, $CO_2$ drawdown is greatly influenced by mineral dissolution rates, which vary by orders of magnitude amongst minerals that have been considered for $CO_2$ sequestration and were examined in this study (Fig. 8; Power et al., 2013).

The log dissolution rates for brucite, wollastonite, forsterite, diopside, and chrysotile (a serpentine polymorph) are -11.5, -12.5, -13.8, -15.0 and -15.5 mol/$cm^2/s$ at the pH of the deionized water used in

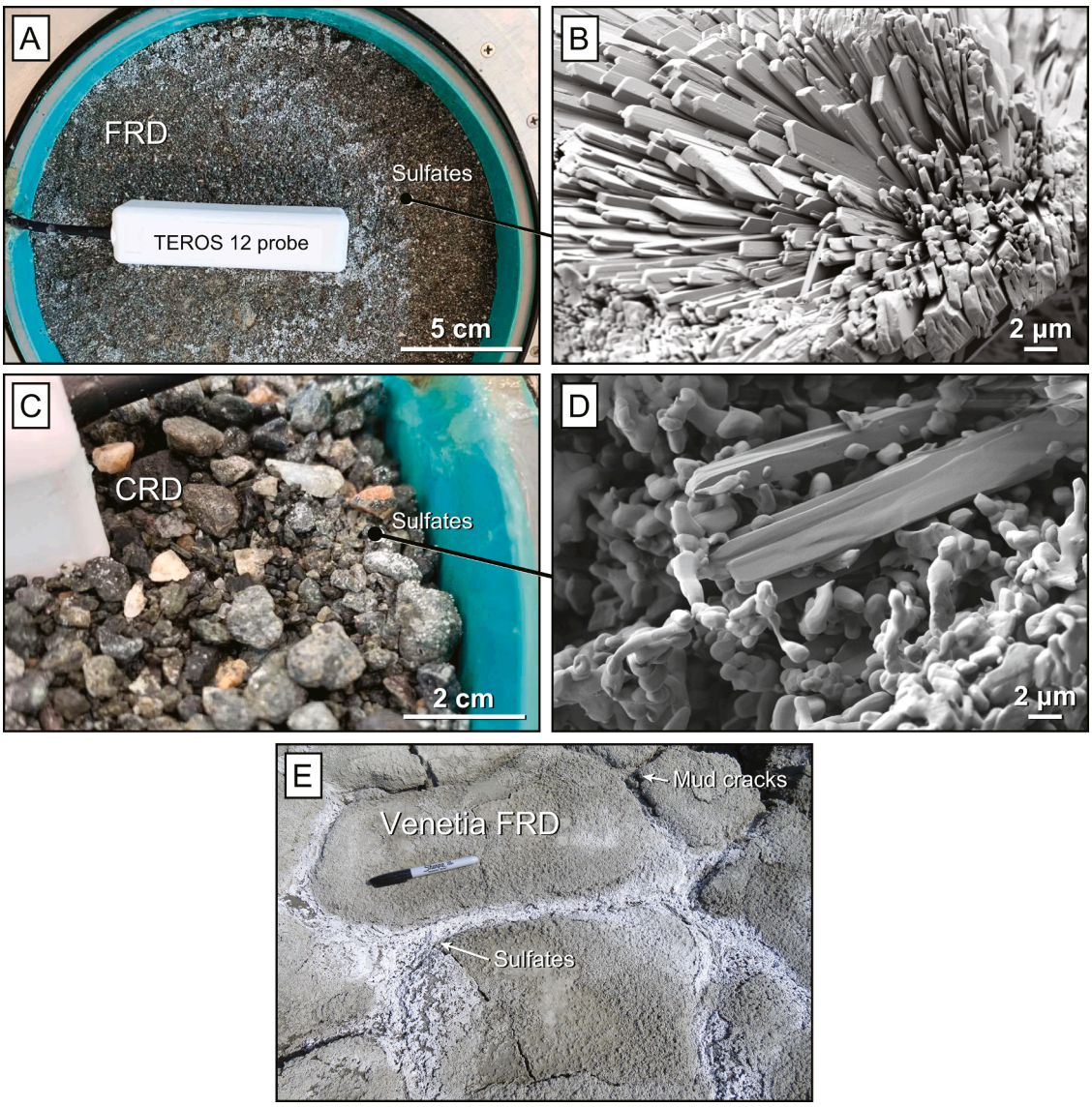


**Fig. 7.** Photographs of Venetia kimberlite residues used in experiments. **A:** White efflorescences formed on the surface of the FRD. TEROS 12 probes measured volumetric water content, conductivity, and temperature. **B:** SEM micrograph of a secondary efflorescence on the FRD surface that was identified as a sulfate mineral using EDS. **C:** White efflorescences formed on the surface of CRD. **D:** SEM micrograph of secondary sulfates on the surface of CRD. **E:** For comparison, sulfate precipitates on the surface of fine kimberlite residues at Venetia Diamond Mine (marker for scale).

experiments (pH = 5.6), respectively (Fig. 8; e.g., Pokrovsky and Schott, 2000, 2004; Pokrovsky et al., 2009; Power et al., 2013; Thom et al., 2013). The wollastonite skarn contained a major abundance of diopside (41.0 wt.%) that has much slower dissolution rates than wollastonite (Fig. 8). Consequently, wollastonite (21.6 wt.%) was likely the major contributor to the drawdown of $CO_2$ in the experiment. Minerals with faster dissolution rates such as brucite will buffer solution pH more than less reactive phases. As approximations of pore water pH, slurries of the brucite-quartz mixture, forsterite, wollastonite skarn, serpentinite, and quartz had pH values of 9.98, 9.23, 8.83, 8.11, and 7.8, respectively, which is indicative of their bulk mineral dissolution rates. These pH values were reasonably well estimated using PHREEQC (Parkhurst and Appelo, 2013) except for quartz that showed greater buffering likely due to the presence of trace carbonate cement as indicated by TIC data (16 ppm C). The most negative $CO_2$ fluxes were achieved using sediments with faster dissolving minerals (e.g., brucite), capable of greater pH buffering. Paulo et al. (2021) tested the reactivity of these same feedstocks using batch $CO_2$ leaches and found that brucite ore was the most reactive material followed by wollastonite skarn, forsterite and serpentinite, which is consistent with $CO_2$ fluxes measured in this study.

Relatively inert quartz sand exhibited overall positive $CO_2$ fluxes, which were also affected by diurnal temperature fluctuations at the end of the experiment (Fig. 4A). Negative fluxes were recorded for all other experiments after water addition due to mineral dissolution and buffering of pore water pH. Single-hydroxide minerals (e.g., brucite) generally dissolve orders of magnitude faster than multi-oxide minerals (e.g., forsterite; Fig. 8); however, for short periods some silicates (e.g., serpentine minerals) may dissolve more rapidly due to easily extractable (labile) cations on mineral surfaces (Power et al., 2020; Vanderzee et al., 2019). In this study, brucite-quartz mixtures exhibited similar fluxes (e.g., -630 g $CO_2/m^2/yr$) to the forsterite sand (e.g., -500 g $CO_2/m^2/yr$) immediately after the addition of water. These two feedstocks achieved similar initial drawdown rates despite very different dissolution rates due to the reaction of labile Mg. Vanderzee et al. (2019) define labile Mg as being easily extractable such as from the dissolution of highly reactive phases (e.g., brucite) and release of loosely bonded Mg ions from silicate surfaces (e.g., forsterite and serpentine polymorphs). Each consecutive wetting of the forsterite sand resulted in less $CO_2$ drawdown. This

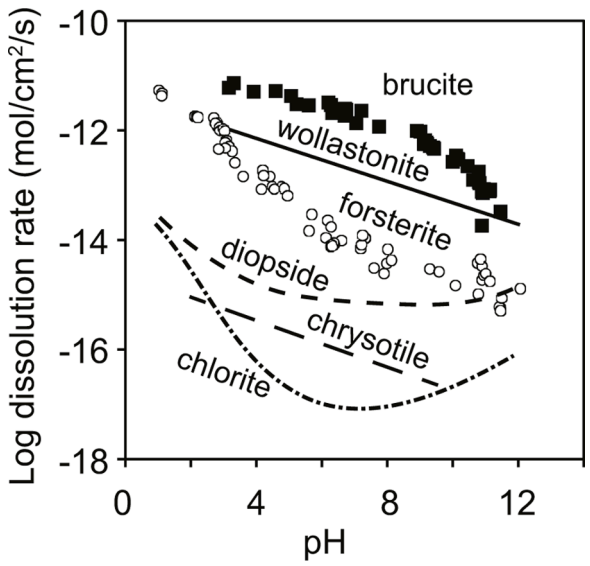


**Fig. 8.** Dissolution rate (log) versus pH for brucite, wollastonite, forsterite, diopside, chrysotile, and chlorite (Modified from Power et al., 2013). Dissolution rates for diopside and chlorite were added from Declercq and Oelkers (2014).

finding can be attributed to a loss in reactivity as labile Mg ions were stripped from surfaces (Power et al., 2020; Thom et al., 2013). Conversely, fluxes became more negative in the brucite experiment until day 7 (Fig. 5A) given that brucite is itself a source of labile Mg, which did not become exhausted during the experiment. Thus, exposing the labile component of more recalcitrant phases will yield a greater drawdown in $CO_2$ and prevent loss in reactivity.

Serpentinite sediments also showed an initial drawdown of $CO_2$ likely owing to pH buffering caused by labile Mg dissolution (Fig. 4C). Similarly, Power et al. (2020) demonstrated that the majority of Mg released from serpentinite with trace to major abundances of brucite (<1–10 wt.%) occurred rapidly in flow-through leaching experiments due to the release of Mg ions on serpentine surfaces (Thom et al., 2013) and complete dissolution of brucite. The labile component of these samples cannot be regenerated, as was observed in the forsterite experiment where reactivity was not regained during subsequent wetting periods (Fig. 4B). Preferential release of Mg during olivine dissolution can form silica-rich layers that passivate surfaces and slow dissolution rates (Daval et al., 2011; Pokrovsky and Schott, 2000; Rosso and Rimstidt, 2000). Serpentine dissolves approximately two orders of magnitude slower than forsterite (Fig. 8). This difference in dissolution rates was compensated by serpentine having a greater specific surface area (25.30 $m^2/g$) than the forsterite sediments (1.14 $m^2/g$; Table 3), which equates to more labile Mg being available for carbonation reactions.

Labile Ca is also of interest for $CO_2$ mineralization. The skarn was a mixture of wollastonite (21.6 wt.%) and less reactive and more abundant diopside (41.0 wt.%; Fig. 8). The most negative flux was recorded immediately after water addition due to the reactivity of labile Ca. Although diopside may have provided labile Mg and Ca from its surfaces, the more reactive wollastonite was likely the leading cause of $CO_2$ drawdown. Targeting surface cations allows for an initial drawdown in $CO_2$ for recalcitrant silicate phases; however, this reactivity cannot be maintained for extended periods.

### 5.2. *Effect of permeability, water, and temperature on $CO_2$ fluxes*

Water content and permeability play a crucial role in $CO_2$ fluxes. Water is required for mineral dissolution, hydration of $CO_2$, and precipitation of hydrated carbonate minerals. Thus, carbonation rates can be limited in low water conditions (Assima et al., 2013; Harrison et al., 2015), while too much water decreases permeability limiting $CO_2$ ingress (Wilson et al., 2011). Grain size also affects permeability (Earle, 2015) and $CO_2$ supply, that latter being a rate-limiting factor in the carbonation of reactive phases such as brucite (Power et al., 2013).

In the flat brucite-quartz experiments, $CO_2$ fluxes became more negative as the sediment dried, which can be explained by the increase in permeability as porewater evaporated (Fig. 5A). Other studies have shown that brucite carbonation is $CO_2$ supply limited (Harrison et al., 2013; Power et al., 2016; Wilson et al., 2010, 2014) as it has a rapid dissolution rate (Fig. 8) compared to more recalcitrant Mg-silicate minerals. After reaching the most negative flux on day 7, fluxes became less negative due to insufficient water. The optimal water content of 14–33% saturation determined in this study differs from previous brucite carbonation studies. For instance, Assima et al. (2013) and Harrison et al. (2015) found that the ideal water content for brucite carbonation ranged from 30 to 60%, however, $CO_2$ injection methods were used which differs from this study.

The relative permeability of mineral wastes with respect to the gas phase is known to change depending on the degree of saturation, whereby lower water content can increase $CO_2$ ingress (Fernandez Bertos et al., 2004). In brucite carbonation microfluidics experiments, Harrison et al. (2017) noted that the gas-water interface tends to increase as evaporation progresses. As brucite-quartz sediments dried, the gas-water interface would have increased, allowing for greater $CO_2$ uptake from the gas phase into pore waters as measured by the $CO_2$ flux analyzer. However, this interface would have decreased upon further drying, and there would have been insufficient water for carbonation reactions. Hence, $CO_2$ fluxes became less negative (Fig. 5A).

Tilling also had an impact on water saturation and $CO_2$ supply. In the tilled brucite-quartz experiment, initial fluxes were greater than twice those observed in the flat experiments due to increased $CO_2$ supply (Fig. 5B). Tilling improves aeration (Buragiene et al., 2019) but also promotes evaporation. Consequently, fluxes became less negative due to water loss towards the end of the experiment. Similarly, the tilled wollastonite experiment exhibited more negative fluxes than the flat experiments. Water content reached nearly dry conditions in tilled experiments (11%) two days earlier than those with a flat surface (13%), demonstrating that increasing exposure to the atmosphere accelerates evaporation and subsequent $CO_2$ drawdown.

The weathering and carbonation of recalcitrant silicate minerals are limited by the rate of cation release, i.e., mineral dissolution (Power et al., 2013; Schott et al., 2009). Forsterite (Fig. 4B) and serpentinite (Fig. 4C) experiments exhibited the most negative fluxes immediately after water addition. Furthermore, $CO_2$ fluxes returned to more negative values in response to each water addition during the wetting and drying cycles of the forsterite experiments. This response is a result of more forsterite dissolution and subsequent release of Mg. The rate of weathering of these minerals depends not only on mineralogy and reactive surface area but also the water-rock ratio, which was greatest immediately after wetting (Brantley and Mellott, 2000; Helgeson et al., 1984; White and Brantley, 2003). In other words, the greater water-rock ratios at the beginning of the experiments allowed for greater mineral dissolution, pH buffering, and $CO_2$ drawdown.

Laboratory temperature varied during the $CO_2$ flux experiments, ranging between 19 and 32 °C with the coolest temperatures during fall months and the warmest during summer months. Relative humidity ranged from 8 to 85%, with lower humidity in the winter and the highest in the summer. Generally, cooler temperatures were recorded mid-morning and warmer temperatures in the early evening. These diurnal fluctuations caused $CO_2$ fluxes to vary towards the end of experiments with less reactive material (e.g., forsterite; Fig. 4B). Conversely, temperature did not affect strongly negative fluxes that occurred when the water content was high or for more reactive feedstocks.

### 5.3. Solubility versus mineral trapping of $CO_2$

Solubility trapping of $CO_2$ refers to its storage as a dissolved phase (e.g., $HCO_3$-), whereas mineral trapping or mineralization of $CO_2$ involves storage within carbonate minerals (Gilfillan et al., 2009). In experiments, negative fluxes were measured for all materials after water addition with the exception of quartz, demonstrating the removal of $CO_2$ from the atmosphere. The $CO_2$ flux analyzer measures the change in $CO_2$ concentration in the chamber, which is the drawdown of $CO_2$ from the atmosphere into pore waters, i.e., solubility trapping of $CO_2$ (Eq. 1). Mineral trapping of $CO_2$ was determined by measuring the increase in TIC and detection of secondary carbonates using XRD and will only occur if pore waters become saturated and precipitate a carbonate mineral. In the quartz experiment, positive $CO_2$ fluxes may have resulted from the dissolution of minor carbonate cement.

$CO_2$ fluxes remained negative throughout the brucite-quartz and wollastonite skarn experiments (Figs. 9A and B), indicating a net removal of $CO_2$. Based on TIC and XRD data, approximately 3.3 (0 to +11.6 g $CO_2$) and 7.1 g $CO_2$ (0 to +28.2 g $CO_2$) was stored as hydromagnesite and calcite owing to the carbonation of brucite (Eq. 13) and wollastonite (Eq. 14), respectively.

$$5Mg(OH)_{2(s)} + 4CO_2 \rightarrow Mg_5(CO_3)_4(OH)_2{\cdot}4H_2O_{(s)} \quad (13)$$

$$CaSiO_{3(s)} + CO_2 \rightarrow CaCO_{3(s)} + SiO_2 \quad (14)$$

Fluxes during brucite-quartz experiments corroborate these results with a net removal of 1.6 g of $CO_2$. In the flat and tilled wollastonite experiments, a net removal of 0.12 and 0.13 g $CO_2$ was achieved; however, these results were inconsistent with changes in TIC [0.04% (0 to +0.16%)]. This discrepancy is likely due to the heterogeneity of the wollastonite skarn sediments, making it challenging to determine the overall change in TIC accurately.

$CO_2$ fluxes for the forsterite and flat serpentinite experiments became positive on days 7 and 5 when water saturation decreased below 50% and 25%, respectively. Tilled serpentinite reached positive values after day 2 at 22% saturation. Maximum positive fluxes reached 470, 250, and 730 g $CO_2/m^2/yr$ for forsterite, flat serpentinite, and tilled serpentinite, respectively (Figs. 4B and C). In the forsterite experiments, there was a removal of 0.04 g $CO_2$; however, no increase in TIC was detected. The flat serpentinite experiment removed 0.01 g $CO_2$ while the tilled experiment lost 0.19 g $CO_2$. No changes were detected in TIC, indicating that no secondary minerals precipitated or these were below the detection limit. Results suggest that $CO_2$ had been stored as a soluble phase (e.g., $HCO_3$-) under high water content but was degassed as evaporation progressed. By combining $CO_2$ flux and TIC measurements, we distinguished between solubility and mineral trapping, which will improve carbon accounting.

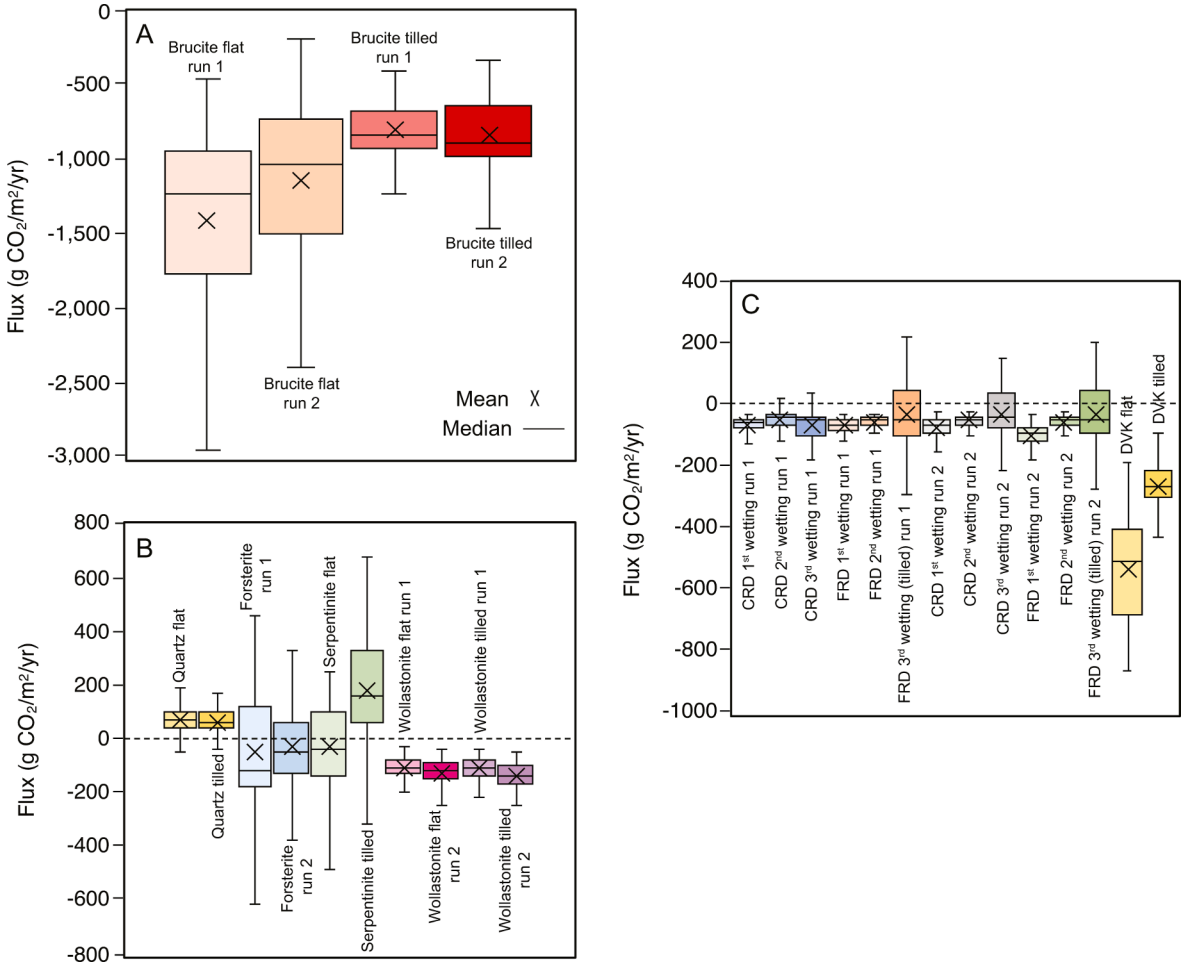


**Fig. 9.** Range in $CO_2$ fluxes (g $CO_2/m^2/yr$) for powdered rocks and Venetia residues. The graphs show the variability in fluxes for the experiments using **A:** brucite-quartz mixture (flat and tilled), **B:** quartz (flat and tilled), forsterite, serpentinite (flat and tilled), and wollastonite (flat and tilled), and **C:** Venetia FRD, CRD, and DVK samples. The mean and median in each dataset is represented by an *X* and black line within box plot. The top quartile of the data (Q3) is the upper half of the box and the bottom quartile (Q1) is the lower half. Minimum and maximum measurements are represented by whiskers.

### 5.4. $CO_2$ sequestration at the Venetia diamond mine

#### 5.4.1. Suitability and capacity of kimberlite residues

In 2016, Venetia emitted 210,000 t of $CO_2$e and treated 4.74 Mt of ore (Mervine et al., 2018), creating a substantial amount of processed kimberlite that can be used as a feedstock for ERW and $CO_2$ mineralization (Mervine et al., 2018; Power et al., 2014; Rollo and Jamieson, 2006; Wilson et al., 2011). Venetia kimberlite contains desirable minerals for $CO_2$ sequestration, including lizardite, diopside, and clinochlore, that may contribute Ca and Mg required for secondary carbonate precipitation. Of these target minerals, lizardite likely has the greatest potential for $CO_2$ mineralization due to its Mg content, faster dissolution rates (Fig. 8), and high surface area (Power et al., 2014, 2013). For example, Wilson et al. (2009a) identified secondary hydrated magnesium carbonates resulting from the weathering of mine wastes dominated by serpentine minerals. Fewer studies have focused on diopside and clinochlore carbonation; however, these minerals have been identified in peridotite and serpentinite studied for $CO_2$ sequestration (Beinlich et al., 2012; Kelemen et al., 2011; Meyer et al., 2014; O'Connor et al., 2002).

Venetia has a maximum capacity to offset 0.84–1.47 Mt $CO_2$ assuming complete carbonation of the CaO and MgO within the 4.74 Mt of kimberlite residues to form carbonate minerals with a 1:1 molar ratio with C. However, ERW and $CO_2$ mineralization rates will mainly be limited by mineral dissolution, residue storage conditions, and climate. For instance, Paulo et al. (2021) tested the reactivity of the CRD and FRD residues and pulverized DVK ore and found these to have the potential to sequester 9, 7, and 5 kg $CO_2$/t residues, respectively, based on the release of easily extractable cations from non-carbonate sources. This portion of the $CO_2$ sequestration capacity is likely the most accessible, and therefore, should be targeted when implementing strategies to enhance passive carbonation.

#### 5.4.2. Evidence of passive carbonation at Venetia

Process waters are recovered from the FRDs and are circulated back to the ore processing circuit. This reuse of process water in an arid climate allows for evapoconcentration of ions (e.g., $Ca^{2+}$ and $CO_3^{2-}$) that likely leads to secondary mineral precipitation. Fine residues often become lightly cemented at the surface due to drying and readily fizz with dilute HCl acid, indicating the presence of fine-grained carbonate. Similarly, other studies have documented secondary carbonate formation within mine wastes being driven by evaporation (Acero et al., 2007, 2009; Bea et al., 2012; Wilson et al., 2014). In addition, white sulfate efflorescences are commonly seen on the surface of dry fine residues (Fig. 7E). The presence of more soluble sulfate minerals suggests that pore waters are saturated with respect to less soluble carbonate minerals (e.g., calcite).

Venetia process waters are supersaturated with respect to calcite yet undersaturated with respect to hydrated Mg-carbonates. However, it is difficult to distinguish between primary and secondary calcite using techniques such as XRD. Furthermore, newly precipitated carbonate that is less than ~0.5 wt.% or is a hydrated Mg-carbonate will unlikely be detected by XRD due to low abundance and poor crystal structure. Wilson et al. (2011) used XRD methods to quantify the abundance of nesquehonite ($MgCO_3{\cdot}3H_2O$) to determine the rates of $CO_2$ removal within kimberlite mine wastes at the Diavik Diamond Mine, Northwest Territories, Canada. This hydrated Mg-carbonate is known to only form at or near Earth's surface conditions (Königsberger et al., 1999) and would not be present as a primary phase in kimberlite ore. Other studies have also relied on extensive sampling and quantitative mineralogy to estimate passive carbonation rates occurring within ultramafic mine wastes (Turvey et al., 2018; Wilson et al., 2011, 2014). For instance, nearly 1000 samples were required to estimate the passive carbonation rate within the tailings impoundment (~16.6 $km^2$) at the Mount Keith Nickel Mine, Western Australia, using quantification of hydrated Mg-carbonates and their carbon isotopic signatures (Wilson et al., 2014). $CO_2$ flux measurements may provide an alternate method for assessing passive carbonation at mines such as Venetia.

#### 5.4.3. Direct measurement of $CO_2$ uptake into kimberlite residues

Experimental results show that mineralogy and the degree of pore water saturation have the most influence on $CO_2$ fluxes. The Venetia kimberlite residues contain a variety of alkaline silicates (Table 4) that may buffer pH and contribute dissolved Mg and Ca that are needed for carbonate precipitation. Serpentine and diopside are the two minerals common between the powdered rocks and Venetia residues used in this study. CRD and FRD experiments showed logarithmic trends in $CO_2$ flux values (Figs. 6A and B) similar to those in the serpentinite experiments (Fig. 4C), where the most negative fluxes were observed immediately after the first wetting and then increased as evaporation progressed. Similar to the forsterite experiments, $CO_2$ fluxes became less negative in the FRD and CRD as water was added due to the loss of labile cations. Water saturation for the tilled FRD was underestimated due to poor contact with the probe, similar to the tilled wollastonite experiment.

The mineralogical composition of CRD and FRD residues were similar (Table 4), yet the physical properties showed substantial differences that impacted the drawdown of $CO_2$. The CRD residues were much coarser than the FRD residues, which enhanced their permeability and facilitated $CO_2$ ingress. Despite the substantial difference in particle sizes, specific surface areas for the CRD and FRD were similar at 5.80 and 7.70 $m^2$/g, respectively. These surface areas and dominated by clay minerals, and therefore, do not represent the reactive surface area of the target minerals (serpentine, diopside, and clinochlore). However, it is still expected that the finer residues are more reactive, yet $CO_2$ ingress is hindered by lower permeability.

The white efflorescences, sampled from the surfaces of the FRD (Figs. 7A and B) and CRD (Figs. 7C and D) residues, were identified as sulfates using EDS. Precipitation of non-carbonate minerals may decrease $CO_2$ sequestration potential as these minerals use valuable cations required for carbonate precipitation. In environments where both sulfates and carbonates are detected, it is likely a result of differences in water content and evaporation rates. Evaporite minerals such as sulfates (Jambor et al., 2000) are commonly more soluble than carbonates and require nearly dry conditions to form, similar to conditions towards the end of experiments in this study. No changes were detected in TIC in the FRD experiment. The CRD material was too coarse and heterogeneous to accurately detect any small changes in TIC to confirm the storage of $CO_2$ via mineral trapping. The initial negative $CO_2$ fluxes reflect momentary solubility trapping before evaporation and $CO_2$ degassing in the MVK-dominated CRD and FRD. These results highlight the limitations of using TIC to assess $CO_2$ removal.

Although DVK lacked any highly reactive phases, it showed similar $CO_2$ drawdown trends as the brucite-quartz experiments. Negative fluxes were recorded immediately after water addition; however, the greatest period of $CO_2$ drawdown was from days 1 to 4 as sediments dried from 54% to 41% saturation. The most negative flux of -870 g $CO_2/m^2$/yr occurred between days 2 and 3. Although this rate differs from the brucite-quartz experiment, similar parabolic patterns were observed. The reactivity of DVK is best explained by the presence of easily extractable cations on mineral surfaces that had not been removed by process water, as was the case for the CRD and FRD. For comparison, DVK consumed over three times the amount of $CO_2$ compared to CRD and FRD (Fig. 9C). However, $CO_2$ fluxes were not nearly as negative after the second water addition (Fig. 5G). The FRD, CRD, and DVK experiments showed that repeated wettings caused fluxes to become less negative due to the loss of easily extractable cations.

## 6. Implications for enhanced rock weathering and $CO_2$ mineralization

In this study, $CO_2$ fluxes were comparable to other approaches for measuring $CO_2$ removal, which are more time and labor intensive

(Wilson et al., 2011, 2014). For less reactive materials, fluxes were at times low and fluctuated due to temperature variations, indicating that measurements were at or approaching the instrument's detection limit. In these circumstances, additional monitoring approaches should be utilized. Coupling $CO_2$ flux measurements with additional data such as TIC and quantitative mineralogy can provide evidence for mineral trapping, a long-term sink for $CO_2$. However, if the feedstock is too coarse, as was the case for the CRD residues from Venetia, and has a highly variable carbon content, then TIC changes may not be detectable. With the ability to rapidly measure $CO_2$ drawdown, $CO_2$ sequestration can be monitored over time with certainty and efficiency in more reactive feedstocks such as brucite-bearing tailings, wollastonite skarn, or unweathered ultramafic mine wastes.

The mining industry will play an essential role in developing enhanced rock weathering and $CO_2$ mineralization at their mines or supplying powdered alkaline rock for off-site use. Annually, ~419 Mt of ultramafic and mafic mine tailings are produced that have substantial potential to sequester $CO_2$ (Power et al., 2014, 2013). Bullock et al. (2021) estimates that between all deposit types, primarily from mafic and ultramafic rocks and Cu-hosting deposits, there is the potential to sequester ~1.1–4.5 Gt $CO_2$ annually. The use of existing mine wastes (e.g., tailings and residues) reduces the overall cost of ERW as mining and processing of rock has already occurred (Strefler et al., 2018).

The feedstocks tested in this study have mineral dissolution rates that vary by orders of magnitude (Fig. 8) and, as a result, will achieve variable rates of $CO_2$ sequestration. Weathering of recalcitrant silicate minerals is limited by dissolution and can be enhanced by having a greater fluid:rock ratio as was demonstrated in the forsterite and serpentinite experiments. Practically, this enhancement would be achieved by spreading powdered rock out over larger areas (Renforth, 2012; Schuiling and Krijgsman, 2006, and references therein), thus exposing it to more reactive fluid (i.e., carbonic acid in rainwater). Dispersal of these feedstocks in various environments has been proposed, including croplands (Beerling et al., 2018; Haque et al., 2019; van Straaten, 2007), coastal areas (Hangx and Spiers, 2009), seawater (Rigopoulos et al., 2018), and at mines (Wilson et al., 2011, 2014). For example, Turvey et al. (2018) estimated a $CO_2$ removal rate of 230–405 g $CO_2/m^2/yr$ at the Woodsreef Chrysotile Mine in New South Wales, Australia, similar to the most negative flux measured in the serpentinite experiment (-260 g $CO_2/m^2/yr$). If practically and environmentally responsible, greater dispersal of mine wastes on- or off-site would allow for greater exposure to rainfall (i.e., dilute carbonic acid), thereby enhancing rates of $CO_2$ sequestration.

Dispersing highly reactive phases such as brucite will also enhance $CO_2$ removal. The most negative $CO_2$ flux measured in the brucite experiment was -2940 g $CO_2/m^2/yr$, which is consistent with an experimental weathering study by Power et al. (2020) and a field study by Wilson et al. (2014) that determined $CO_2$ removal rates of -3500 and -2400 g $CO_2/m^2/yr$ in brucite-bearing ultramafic tailings, respectively. McQueen et al. (2020) proposed enhanced weathering using recycled magnesite calcined to produce highly reactive magnesia (MgO). The authors recommend dispersing magnesia as a 10 cm layer and suggest this material will completely react to form magnesite within a year, providing a $CO_2$ sequestration rate of -160,000 g $CO_2/m^2/yr$. Reaction rates were based on brucite dissolution experiments (e.g., Pokrovsky and Schott, 2004); however, the $CO_2$ removal rate is approximately 50 times faster than the fastest rate measured in brucite experiments from this study (-2940 g $CO_2/m^2/yr$). Brucite carbonation is limited by $CO_2$ supply (Harrison et al., 2013; Wilson et al., 2014) or, more practically, the ingress of atmospheric $CO_2$ into the porous sediments. Furthermore, $CO_2$ fluxes in this study became less negative as sediments dried, and thus, brucite and magnesia will be much less efficient at removing $CO_2$ under dry conditions. $CO_2$ flux analyzers could be deployed in the scenario proposed by McQueen et al. (2020) for real-time monitoring of $CO_2$ removal.

ERW and $CO_2$ mineralization may be deployed at the mine site. Passive carbonation has been documented at several mines, including Woodsreef (Oskierski et al., 2013; Turvey et al., 2018), Clinton Creek (Wilson, 2006; Wilson et al., 2009a), Mount Keith (Bea et al., 2012; Wilson et al., 2014), and Diavik (Wilson et al., 2011, 2009b). Extrapolating the most negative fluxes from experiments to the Venetia FRD and CRD storage facilities suggests maximum passive carbonation rates of ~630 and 70 t $CO_2$/yr can be achieved, respectively. The maximum flux for the pulverized DVK, which is expected to be the dominant kimberlite facies being mined for future production at Venetia, equates to a maximum $CO_2$ sequestration rate of ~3045 t $CO_2$/yr (~1.5% offset) for the FRD impoundments. These rates assume that the entire area of the FRD impoundments is utilized at ideal water saturation.

At Venetia, the deposition of fine residues is alternated between FRD1 and FRD2, where the inactive impoundment becomes dry in the upper few 10′s of centimeters. This scenario is not ideal because the lack of water hinders mineral dissolution and subsequent carbonation reactions, as was noted in our experiments. Conversely, deposition in the active impoundment causes ponding which limits the drawdown of $CO_2$ due to pore spaces being completely filled with water (Wilson et al., 2011). Similarly, the ingress of $CO_2$ was limited at high water content (i.e., low permeability) in the DVK experiments, but as evaporation progressed, there was a greater drawdown of $CO_2$ with the most negative flux recorded at 40% saturation. The initial pore water content of the residues at Venetia is 100%, as these are deposited as a slurry. Allowing residues to dry through the range of ideal water content (60% to 30%) would optimize $CO_2$ sequestration. Therefore, we recommend that both of the impoundments at Venetia be simultaneously utilized to make use of the entire FRD area while keeping water saturation at optimal levels by reducing ponding through improved drainage and minimizing desiccation by more frequent slurry deposition.

Exposing reactive mineral surfaces that contain easily extractable cations (e.g., surface Mg) is needed to achieve greater $CO_2$ drawdown rates. If the fine residues at Venetia were distributed at the same thickness as experiments (8.5 cm), the mine would need to deposit its residues six times per year over the entire FRD area (3.5 $km^2$). This management practice would allow 65 days of reaction, a sufficient period to react easily extractable cations. We recommend more frequent and thinner slurry flows to increase residue exposure and better control water content.

The greatest $CO_2$ drawdowns using CRD were recorded at the beginning of the experiments when water saturation was highest (60%; Fig. 6). The mine could attempt to maintain the water supply within the CRD while also exposing fresh surfaces as repeated wetting causes a loss in reactivity. The high permeability of these residues would allow for repeated leaching, possibly through the circulation of water, to enhance mineral dissolution, but would likely have a negative impact on the mine's water budget.

Mine waste impoundments are designed for containment and, in most cases, to prevent exposure and weathering. The Venetia fine residues are contained in relatively small impoundments, which limits $CO_2$ removal. For comparison, the tailings impoundment at the Mount Keith Nickel Mine is nearly five times the size (16.6 $km^2$) of Venetia's FRDs (~3.5 $km^2$). If Venetia were to disperse residues over an area equivalent to the impoundment at Mount Keith, there would be the potential to offset ~7% of their annual $CO_2$ emissions based on the most negative flux recorded in DVK experiments. This comparison highlights the need to disperse residues at the mine or offsite locations more widely.

## 7. Conclusion

Directly measuring $CO_2$ fluxes is an effective tool for assessing $CO_2$ removal rates in different mine wastes and rock powders. This method allows for high-resolution and real-time measurements of $CO_2$ influx and efflux and can be deployed at mines or ERW application sites. The mineralogical composition of feedstocks has the greatest impact on $CO_2$ fluxes, followed by water content, which should be optimized to

enhance $CO_2$ drawdown. For many feedstocks, $CO_2$ fluxes were most negative following water addition but became positive as drying progressed or when feedstocks failed to regain their initial reactivity after the repeated wettings. This loss in reactivity is attributed to the removal of labile cations. Targeting the labile component in recalcitrant silicates provides rapid initial dissolution rates, enhancing $CO_2$ drawdown. Coupling fluxes with total inorganic carbon data helps differentiate between mineral and solubility trapping of $CO_2$. Modifying management practices at an active mine to increase residue exposure time, expand the dispersal area, and optimize water saturation will lead to greater $CO_2$ removal. Dispersal of mine wastes offsite over large areas in an ERW approach would allow longer reaction times to access a greater portion of the large $CO_2$ sequestration capacity of these residues held within the recalcitrant silicates.

## Declaration of Competing Interest

The authors declare that they have no known competing financial interests or personal relationships that could have appeared to influence the work reported in this paper.

## Acknowledgements

We acknowledge the funding provided by De Beers Group Services and the assistance and support from Evelyn Mervine and Zandile Miya while sampling at the Venetia Diamond Mine. Thank you to Bob Vasily from Canadian Wollastonite for supplying the wollastonite amendment. We are grateful for funding provided by the Natural Sciences and Engineering Research Council of Canada Discovery and Canada Research Chairs programs as well as a Natural Resources Canada Clean Growth grant and Mitacs Accelerate grant to Power and Wilson. We appreciate the expert handling of our manuscript by Associate Editor, Charles Jenkins, and the two anonymous reviewers for their constructive comments.

## Supplementary materials

Supplementary material associated with this article can be found, in the online version, at doi:10.1016/j.ijggc.2021.103554.

## References

Acero, P., Ayora, C., Carrera, J., 2007. Coupled thermal, hydraulic and geochemical evolution of pyritic tailings in unsaturated column experiments. Geochim. Cosmochim. Acta 71, 5325–5338.
Acero, P., Ayora, C., Carrera, J., Saaltink, M.W., Olivella, S., 2009. Multiphase flow and reactive transport model in vadose tailings. Appl. Geochem. 24, 1238–1250.
Ahirwal, J., Maiti, S.K., Singh, A.K., 2017. Changes in ecosystem carbon pool and soil $CO_2$ flux following post-mine reclamation in dry tropical environment. India. Sci. Total Environ. 583, 153–162.
Assima, G.P., Larachi, F., Beaudoin, G., Molson, J., 2012. $CO_2$ sequestration in chrysotile mining residues—implication of watering and passivation under environmental conditions. Ind. Eng. Chem. Res. 51, 8726–8734.
Assima, G.P., Larachi, F., Beaudoin, G., Molson, J., 2013. Dynamics of carbon dioxide uptake in chrysotile mining residues – Effect of mineralogy and liquid saturation. Int. J. Greenh. Gas Control 12, 124–135.
Assima, G.P., Larachi, F., Molson, J., Beaudoin, G., 2014. Impact of temperature and oxygen availability on the dynamics of ambient $CO_2$ mineral sequestration by nickel mining residues. Chem. Eng. J. 240, 394–403.
Bea, S.A., Wilson, S., Mayer, K.U., Dipple, G.M., Power, I.M., Gamazo, P., 2012. Reactive transport modeling of natural carbon sequestration in ultramafic mine tailings. Vadose Zone J. 11.
Beaudoin, G., Nowamooz, A., Assima, G.P., Lechat, K., Gras, A., Entezari, A., Kandji, E.H. B., Awoh, A.-S., Horswill, M., Turcotte, S., Larachi, F., Dupuis, C., Molson, J., Lemieux, J.-M., Maldague, X., Plante, B., Bussière, B., Constantin, M., Duchesne, J., Therrien, R., Fortier, R., 2017. Passive mineral carbonation of Mg-rich mine wastes by atmospheric $CO_2$. Energy Procedia 114, 6083–6086.
Beerling, D.J., Leake, J.R., Long, S.P., Scholes, J.D., Ton, J., Nelson, P.N., Bird, M., Kantzas, E., Taylor, L.L., Sarkar, B., Kelland, M., DeLucia, E., Kantola, I., Muller, C., Rau, G., Hansen, J., 2018. Farming with crops and rocks to address global climate, food and soil security. Nat. Plants 4, 138–147.
Beinlich, A., Austrheim, H., 2012. In situ sequestration of atmospheric $CO_2$ at low temperature and surface cracking of serpentinized peridotite in mine shafts. Chem. Geol. 332-333, 32–44.
Beinlich, A., Plumper, O., Hovelmann, J., Austrheim, H., Jamtveit, B., 2012. Massive serpentinite carbonation at Linnajavri, N-Norway. Terr. Nova 24, 446–455.
Bish, D.L., Howard, S.A., 1988. Quantitative phase analysis using the rietveld method. J. Appl. Cryst. 21, 86–91.
Brantley, S.L., Mellott, N.P., 2000. Surface area and porosity of primary silicate minerals. Am. Mineral. 85, 1767–1783.
Bullock, L.A., James, R.H., Matter, J., Renforth, P., Teagle, D.A.H., 2021. Global carbon dioxide removal potential of waste materials from metal and diamond mining. Front. Climate 3.
Buragiene, S., Sarauskis, E., Romaneckas, K., Adamaviciene, A., Kriauciuniene, Z., Avizienyte, D., Marozas, V., Naujokiene, V., 2019. Relationship between $CO_2$ emissions and soil properties of differently tilled soils. Sci. Total Environ. 662, 786–795.
Daval, D., Sissmann, O., Menguy, N., Saldi, G.D., Guyot, F., Martinez, I., Corvisier, J., Garcia, B., Machouk, I., Knauss, K.G., Hellmann, R., 2011. Influence of amorphous silica layer formation on the dissolution rate of olivine at 90 °C and elevated $pCO_2$. Chem. Geol. 284, 193–209.
Declercq, J., Oelkers, E.H., 2014. CarbFix Report: PHREEQC mineral dissolution kinetics database.
Earle, S., 2015. Physical Geology. BCcampus, Victoria, B.C.
EASAC, 2018. Negative Emission technolgies: What role in Meeting Paris Agreement targets? German National Academy of Sciences Leopoldina.
Entezari Zarandi, A., Larachi, F., Beaudoin, G., Plante, B., Sciortino, M., 2017. Nesquehonite as a carbon sink in ambient mineral carbonation of ultramafic mining wastes. Chem. Eng. J. 314, 160–168.
Fernandez Bertos, M., Simons, S.J., Hills, C.D., Carey, P.J., 2004. A review of accelerated carbonation technology in the treatment of cement-based materials and sequestration of $CO_2$. J. Hazard Mater. 112, 193–205.
Gilfillan, S.M., Lollar, B.S., Holland, G., Blagburn, D., Stevens, S., Schoell, M., Cassidy, M., Ding, Z., Zhou, Z., Lacrampe-Couloume, G., Ballentine, C.J., 2009. Solubility trapping in formation water as dominant $CO_2$ sink in natural gas fields. Nature 458, 614–618.
Hangx, S.J.T., Spiers, C.J., 2009. Coastal spreading of olivine to control atmospheric $CO_2$ concentrations: a critical analysis of viability. Int. J. Greenh. Gas Control 3, 757–767.
Haque, F., Santos, R.M., Dutta, A., Thimmanagari, M., Chiang, Y.W., 2019. Co-Benefits of wollastonite weathering in agriculture: $CO_2$ sequestration and promoted plant growth. ACS Omega 4, 1425–1433.
Harrison, A.L., Dipple, G.M., Power, I.M., Mayer, K.U., 2015. Influence of surface passivation and water content on mineral reactions in unsaturated porous media: implications for brucite carbonation and $CO_2$ sequestration. Geochim. Cosmochim. Acta 148, 477–495.
Harrison, A.L., Dipple, G.M., Song, W., Power, I.M., Mayer, K.U., Beinlich, A., Sinton, D., 2017. Changes in mineral reactivity driven by pore fluid mobility in partially wetted porous media. Chem. Geol. 463, 1–11.
Harrison, A.L., Power, I.M., Dipple, G.M., 2013. Accelerated carbonation of brucite in mine tailings for carbon sequestration. Environ. Sci. Technol. 47, 126–134.
Helgeson, H.C., Murphy, W.M., Aagaard, P., 1984. Thermodynamic and kinetic constraints on reaction rates among minerals and aqueous solutions. II. Rate constants, effective surface area, and the hydrolysis of feldspar. Geochim. Cosmochim. Acta 48, 2405–2432.
Hill, R.J., Howard, C.J., 1987. Quantitative phase analysis from neutron powder diffraction data using the rietveid method. J. Appl. Cryst. 20, 467–474.
IPCC, 2007. IPCC climate change 2007: synthesis report, an assessment of the intergovernmental panel on climate change. http://www.ipcc.ch/pdf/assessment-report/ar4/syr/ar4_syr.pdf.
Jambor, J.L., Nordstrom, D.K., Alpers, C.N., 2000. Metal-sulfate salts from sulfide mineral oxidation. Rev. Mineral. Geochem. 40, 303–350.
Kelemen, P.B., Matter, J., Streit, E.E., Rudge, J.F., Curry, W.B., Blusztajn, J., 2011. Rates and mechanisms of mineral carbonation in peridotite: natural processes and recipes for enhanced, in situ $CO_2$ capture and storage. In: Jeanloz, R., Freeman, K.H. (Eds.), Annual Review of Earth and Planetary Sciences, Vol 39. Annual Reviews, Palo Alto, pp. 545–576.
Königsberger, E., Königsberger, L.C., Gamsjäger, H., 1999. Low-temperature thermodynamic model for the system $Na_2CO_3$-$MgCO_3$-$CaCO_3$-$H_2O$. Geochim. Cosmochim. Acta 63, 3105–3119.
Larachi, F., Daldoul, I., Beaudoin, G., 2010. Fixation of $CO_2$ by chrysotile in low-pressure dry and moist carbonation: ex-situ and in-situ characterizations. Geochim. Cosmochim. Acta 74, 3051–3075.
Lechat, K., Lemieux, J.M., Molson, J., Beaudoin, G., Hebert, R., 2016. Field evidence of $CO_2$ sequestration by mineral carbonation in ultramafic milling wastes, Thetford Mines, Canada. Int. J. Greenh. Gas Control 47, 110–121.
Levitan, D.M., Hammarstrom, J.M., Gunter, M.E., Seal II, R.R., Chou, I.M., 2009. Mineralogy of mine waste at the vermont asbestos group mine, Belvidere Mountain, Vermont. Am. Mineral. 94, 1063–1066.
McQueen, N., Kelemen, P., Dipple, G., Renforth, P., Wilcox, J., 2020. Ambient weathering of magnesium oxide for $CO_2$ removal from air. Nat. Commun. 11, 10.
Mervine, E.M., Wilson, S., Power, I.M., Dipple, G.M., Turvey, C.C., Hamilton, J.L., Vanderzee, S., Raudsepp, M., Southam, C., Matter, J.M., Kelemen, P.B., Stiefenhofer, J., Miya, Z., Southam, G., 2018. Potential for offsetting diamond mine carbon emissions through mineral carbonation of processed kimberlite: an assessment of De Beers mine sites in South Africa and Canada. Mineral. Petrol.

Meyer, N.A., Vogeli, J.U., Becker, M., Broadhurst, J.L., Reid, D.L., Franzidis, J.P., 2014. Mineral carbonation of PGM mine tailings for $CO_2$ storage in South Africa: a case study. Miner. Eng. 59, 45–51.
Meysman, F.J.R., Montserrat, F., 2017. Negative $CO_2$ emissions via enhanced silicate weathering in coastal environments. Biol. Lett. 13, 7.
Mukhopadhyay, S., Maiti, S.K., 2014. Soil $CO_2$ flux in grassland, afforested land and reclaimed coalmine overburden dumps: a case study. Land Degradat. Dev. 25, 216–227.
NOAA, 2020. Monthly Average Mauna Loa CO2.
O'Connor, W.K., Dahlin, D.C., Rush, G.E., Dahlin, C.L., Collins, W.K., 2002. Carbon dioxide sequestration by direct mineral carbonation: process mineralogy of feed and products. Miner. Metall. Process. 19, 95–101.
Oskierski, H.C., Dlugogorski, B.Z., Jacobsen, G., 2013. Sequestration of atmospheric $CO_2$ in chrysotile mine tailings of the Woodsreef Asbestos Mine, Australia: quantitative mineralogy, isotopic fingerprinting and carbonation rates. Chem. Geol. 358, 156–169.
Parkhurst, D.L., Appelo, C.A.J., 2013. Description of input and examples for PHREEQC version 3—A computer program for speciation, batch-reaction, one-dimensional transport, and inverse geochemical calculations. U.S. Geol. Survey Tech. Methods, p. 497.
Paulo, C., Power, I.M., Stubbs, A.R., Wang, B., Zeyen, N., Wilson, S., 2021. Evaluating feedstocks for carbon dioxide removal by enhanced rock weathering and $CO_2$ mineralization. Appl. Geochem. 129, 104955.
Pokrovsky, O.S., Schott, J., 2000. Kinetics and mechanism of forsterite dissolution at 25 °C and pH from 1 to 12. Geochim. Cosmochim. Acta 64, 3313–3325.
Pokrovsky, O.S., Schott, J., 2004. Experimental study of brucite dissolution and precipitation in aqueous solutions: surface speciation and chemical affinity control. Geochim. Cosmochim. Acta 68, 31–45.
Pokrovsky, O.S., Shirokova, L.S., Benezeth, P., Schott, J., Golubev, S.V., 2009. Effect of organic ligands and heterotrophic bacteria on wollastonite dissolution kinetics. Am. J. Sci. 309, 731–772.
Power, I., McCutcheon, J., Harrison, A., Wilson, S., Dipple, G., Kelly, S., Southam, C., Southam, G., 2014. Strategizing carbon-neutral mines: a case for pilot projects. Minerals 4, 399–436.
Power, I.M., Dipple, G.M., Bradshaw, P.M.D., Harrison, A.L., 2020. Prospects for $CO_2$ mineralization and enhanced weathering of ultramafic mine tailings from the Baptiste nickel deposit in British Columbia, Canada. Int. J. Greenh. Gas Control 94.
Power, I.M., Harrison, A.L., Dipple, G.M., 2016. Accelerating mineral carbonation using carbonic anhydrase. Environ. Sci. Technol. 50, 2610–2618.
Power, I.M., Harrison, A.L., Dipple, G.M., Wilson, S., Kelemen, P.B., Hitch, M., Southam, G., 2013. Carbon mineralization: from natural analogues to engineered systems. Rev. Mineral. Geochem. 77, 305–360.
Power, I.M., Wilson, S., Dipple, G.M., Southam, G., 2011. Modern carbonate microbialites from an asbestos open pit pond, Yukon, Canada. Geobiology 9, 180–195.
Pronost, J., Beaudoin, G., Lemieux, J.M., Hebert, R., Constantin, M., Marcouiller, S., Klein, M., Duchesne, J., Molson, J.W., Larachi, F., Maldague, X., 2012. $CO_2$-depleted warm air venting from chrysotile milling waste (Thetford Mines, Canada): evidence for in-situ carbon capture from the atmosphere. Geology 40, 275–278.
Pronost, J., Beaudoin, G., Tremblay, J., Larachi, F., Duchesne, J., Hebert, R., Constantin, M., 2011. Carbon sequestration kinetic and storage capacity of ultramafic mining waste. Environ. Sci. Technol. 45, 9413–9420.
Renforth, P., 2012. The potential of enhanced weathering in the UK. Int. J. Greenh. Gas Control 10, 229–243.
Rietveld, H.M., 1969. A profile refinement method for nuclear and magnetic structures. J. Appl. Cryst. 2, 65–71.
Rigopoulos, I., Harrison, A.L., Delimitis, A., Ioannou, I., Efstathiou, A.M., Kyratsi, T., Oelkers, E.H., 2018. Carbon sequestration via enhanced weathering of peridotites and basalts in seawater. Appl. Geochem. 91, 197–207.
Rollo, H.A., Jamieson, H.E., 2006. Interaction of diamond mine waste and surface water in the Canadian Arctic. Appl. Geochem. 21, 1522–1538.
Rosen, J., 2018. Vast bioenergy plantations could stave off climate change—And radically reshape the planet. Science.
Rosso, J.J., Rimstidt, J.D., 2000. A high resolution study of forsterite dissolution rates. Geochim. Cosmochim. Acta 64, 797–811.
Schott, J., Pokrovsky, O.S., Oelkers, E.H., 2009. The link between mineral dissolution/precipitation kinetics solution chemistry. Rev. Mineral. Geochem. 70, 207–258.
Schuiling, R.D., Krijgsman, P., 2006. Enhanced weathering: an effective and cheap tool to sequester $CO_2$. Climatic Change 74, 349–354.
Strefler, J., Amann, T., Bauer, N., Kriegler, E., Hartmann, J., 2018. Potential and costs of carbon dioxide removal by enhanced weathering of rocks. Environ. Res. Lett. 13.
Taylor, L.L., Quirk, J., Thorley, R.M.S., Kharecha, P.A., Hansen, J., Ridgwell, A., Lomas, M.R., Banwart, S.A., Beerling, D.J., 2015. Enhanced weathering strategies for stabilizing climate and averting ocean acidification. Nat. Clim. Chang. 6, 402–406.
Thom, J.G.M., Dipple, G.M., Power, I.M., Harrison, A.L., 2013. Chrysotile dissolution rates: implications for carbon sequestration. Appl. Geochem. 35, 244–254.
Turvey, C.C., Wilson, S., Hamilton, J.L., Tait, A.W., McCutcheon, J., Beinlich, A., Fallon, S.J., Dipple, G.M., Southam, G., 2018. Hydrotalcites and hydrated Mg-carbonates as carbon sinks in serpentinite mineral wastes from the Woodsreef chrysotile mine, New South Wales, Australia: controls on carbonate mineralogy and efficiency of $CO_2$ air capture in mine tailings. Int. J. Greenh. Gas Control 79, 38–60.
van Straaten, P., 2007. Agrogeology: The Use of Rocks for Crops. Enviroquest Ltd, Cambridge, Ontario, Canada, p. 440.
Vanderzee, S.S.S., Dipple, G.M., Bradshaw, P.M.D., 2019. Targeting Highly Reactive Labile Magnesium in Ultramafic Tailings For Greenhouse-Gas Offsets and Potential Tailings Stabilization at the Baptiste Deposit. Central British Columbia (NTS 093 K/13, 14), Geoscience BC, pp. 109–118.
White, A.F., Brantley, S.L., 2003. The effect of time on the weathering of silicate minerals: why do weathering rates differ in the laboratory and field? Chem. Geol. 202, 479–506.
Wilson, S., 2006. Verifying and quantifying carbon fixation in minerals from serpentine-rich mine tailings using the Rietveld method with X-ray powder diffraction data. Am. Mineral. 91, 1331–1341.
Wilson, S., Barker, S.L.L., Dipple, G.M., Atudorei, V., 2010. Isotopic disequilibrium during uptake of atmospheric $CO_2$ into mine process waters: implications for $CO_2$ sequestration. Environ. Sci. Technol. 44, 9522–9529.
Wilson, S., Dipple, G.M., Power, I.M., Barker, S.L., Fallon, S.J., Southam, G., 2011. Subarctic weathering of mineral wastes provides a sink for atmospheric $CO_2$. Environ. Sci. Technol. 45, 7727–7736.
Wilson, S., Dipple, G.M., Power, I.M., Thom, J.M., Anderson, R.G., Raudsepp, M., Gabites, J.E., Southam, G., 2009a. Carbon dioxide fixation within mine wastes of ultramafic-hosted ore deposits: examples from the clinton creek and cassiar chrysotile deposits, Canada. Econ. Geol. 104, 95–112.
Wilson, S., Harrison, A.L., Dipple, G.M., Power, I.M., Barker, S.L.L., Ulrich Mayer, K., Fallon, S.J., Raudsepp, M., Southam, G., 2014. Offsetting of $CO_2$ emissions by air capture in mine tailings at the Mount Keith Nickel Mine, Western Australia: rates, controls and prospects for carbon neutral mining. Int. J. Greenh. Gas Control 25, 121–140.
Wilson, S., Raudsepp, M., Dipple, G.M., 2009b. Quantifying carbon fixation in trace minerals from processed kimberlite: a comparative study of quantitative methods using X-ray powder diffraction data with applications to the Diavik Diamond Mine, Northwest Territories, Canada. Appl. Geochem. 24, 2312–2331.